Rock magnetic study of basalt at Lonar impact crater in India: Effects of stress waves on rock magnetic properties

Itoyuki Nishioka

DOCTOR OF
PHILOSOPHY

Department of Polar Science
School of Multidisciplinary Sciences
The Graduate University for Advanced Studies

2007

Abstract

Magnetic anomaly data provide valuable information on size and morphology of buried impact craters. An understanding of how stress waves change magnetic properties of rock is critical for correct interpretation of magnetic data. Although previous studies demonstrated effects of strong shock on magnetic properties of rocks beneath impact craters, effects of relatively weak shock for those of rocks in crater wall have been poorly studied. In this context, we investigated shock effects on magnetic properties through studies of experimentally impacted basaltic andesite, and basalt from natural impact crater (Lonar crater).

An initial peak pressure of 5 GPa was generated in a block of basaltic andesite containing Ti-rich titanomagnetite with the impact of a cylindrical projectile. Effects of decaying stress waves on magnetic properties were subsequently quantified. Natural remanent magnetization (NRM) was partially but significantly demagnetized at peak pressures higher than 1 GPa. High-coercivity part of NRM, even higher than 80 mT, was partially demagnetized. At higher pressure (3-5 GPa), low-field magnetic susceptibility was significantly reduced and coercivity was increased, probably due to increased internal stress. Different patterns of change in anisotropy of magnetic susceptibility (AMS) were observed at different distance from the impacted surface. In high-pressure range (>3 GPa), the anisotropy degree was increased, the minimum susceptibility was oriented toward the shock direction, and the average susceptibility was decreased. This feature is consistent with the result of a previous shock experiment. The initial orientations of AMS were however significantly changed at around 0.4-3 GPa; The maximum susceptibility was induced parallel to the shock direction, and superposed on the initial AMS. This kind of changes in the AMS parameters has been never reported.

Basalt samples were collected from flows in the crater wall, ejecta clasts, and flow outside the rim of Lonar crater. Irreversible thermomagnetic curves

and the maximum Curie temperature of 500-560°C indicated presence of Ti-poor titanomagnetite and its oxidized phase as the main magnetic minerals in Lonar basalts. The result of AMS measurement of both inside and outside samples showed relatively weak anisotropy degree (P<1.03), which is similar to that of basalt from outside the crater rim. The samples from the crater wall showed predominantly oblate shape of AMS ellipsoid, with tightly clustered vertical distribution of the minimum principal axes. Substantial, but not strict, parallelism between the maximum principal axes and the radial direction from the crater center was observed only for the samples from the lower part of the crater wall. This fact and the result of the shock experiment indicate that radially expanding stress waves reoriented the initial AMS.

Stepwise thermal demagnetization of NRM and anhysteretic remanent magnetization (ARM) demonstrated that the main NRM carriers of Lonar basalts are titanomagnetite and titanomaghemite. The primary NRM component was demagnetized above 200°C, indicating that the post-impact temperature did not exceed the value. The site-mean and overall-mean directions were determined for both the high and low coercivity components isolated by stepwise alternating field demagnetization. The intensities of the primary NRM component were generally decreased toward the lower altitude, and positively correlated with the intensity of ARM after AFD with a peak field of 15 mT. This fact indicates that the NRM intensity is not simply a function of distance from the crater center as previously argued. Meanwhile, the site-mean directions of the low-coercivity NRM component were more tightly clustered before tilt correction, and the in-situ overall mean direction was not distinguishable with the present field direction. The ejecta samples also showed two NRM components, whose remagnetization circles intersected at an orientation close to the present earth field. These results suggest that the dominant fraction of the low-coercivity NRM component for the basalt flows in the crater wall and ejecta clasts were not shock remanent magnetization as previously suggested, but were viscous remanent magnetization acquired since the formation of the crater.

Parts of this thesis were published in *Earth Planets and Space* [Nishioka et al., 2007].

Acknowledgements

Initially, I would like to thank my supervisor, Prof. Minoru Funaki of National Institute of Polar Research (NIPR), for his support and guidance throughout the work.

Field trips in India were supported by a number of people. The efficient field logistics were set up by the Geological Survey of India (GSI). I especially thank Dr. K. Venkata Rao for his support and discussions on the various aspects of the research. I thank Dr. K. S. Mishra, Dy. Director General of GSI Central Region, for kindly guiding us at the crater and the surrounding area. I thank Dr. G. V. S. Poornachandra Rao of the National Geophysical Research Institute of India for helpful advice on the research at Lonar.

The shock experiment was conducted using a propellant gun installed at the National Institute for Material Science in Tsukuba. I thank Dr. Toshimori Sekine for his collaboration on the research, which have led to a new result regarding the AMS changes presented in this thesis.

I thank Prof. Yasuhiko Syono of Tohoku University for sharing his insights in rock magnetism and shock experiment. Comments and suggestions by Prof. Naoto Ishikawa of Kyoto University greatly helped to improve this thesis. Profs. Kazuo Shibuya, Yoshifumi Nogi, and Dr. Akira Yamaguchi of NIPR gave me helpful comments regarding my thesis and presentation slides. I also thank Profs. Viktor Hoffmann of University of Tübingen and Mituko Ozima for their valuable discussions on rock magnetic issues.

Contents

Glossary

Abbreviations

AMS	anisotropy of low-field magnetic susceptibility
ARM	anhysteretic remanent magnetization
AFD	alternating field demagnetization
IRM	isothermal remanent magnetization
MD	multidomain
MDF	median destructive field
NRM	natural remanent magnetization
PSD	pseudo-singledomain
SD	singledomain
SRM	shock remanent magnetization
TRM	thermal remanent magnetization
VRM	viscous remanent magnetization

Symbols

ARM_{15} [A m^2/kg]	intensity of ARM after AFD with a peak field of 15 mT
F	AMS foliation (K_2/K_3)
H_c [mT]	coercivity
H_{cr} [mT]	remanence coercivity
I_s [A m^2/kg]	saturation magnetization
I_r [A m^2/kg]	saturation remanent magnetization
K_x (x=1,2,3) [m^3/kg]	the principal low-field magnetic susceptibilities ($K_1 > K_2 > K_3$)
K_m [m^3/kg]	average low-field magnetic susceptibility $(K_1 + K_2 + K_3)/3$
K_p [m^3/kg]	high-field magnetic susceptibility
L	AMS lineation (K_1/K_2)
NRM_{15} [A m^2/kg]	NRM after AFD with a peak field of 15 mT
P	degree of AMS (K_1/K_3)
P_s [GPa]	shock pressure
T_c [°C]	Curie temperature

Chapter 1

General Introduction

1.1 Geophysical signatures of impact craters

Impact craters are dominant landform on many planets, satellites, or other solid body in the Solar System. In contrast, those on earth are less common due to erosion or burial by geologic process such as plate subduction, mountain building, sedimentation, or volcanism. Over 170 impact structures have so far been identified around the world according to Earth Impact Database [2008]. More than 30% of them are inaccessible to direct observation due to burial in post-impact sediments. Geophysical data played a central roll for the initial recognition of these hidden impact craters.

Terrestrial impact structures exhibit characteristic gravity and magnetic signatures [Pilkington and Grieve, 1992]. The most common is a circular gravity low (D<30 km), due to reduction in density by brecciation and post-impact sediment infill. The gravity signature can be modeled well using known morphometric parameters of impact structures. In contrast, magnetic signature is more varied due to larger variation in the magnetic properties of rocks. Magnetic modeling is often difficult due to lack of magnetization data and concepts on impact related magnetization. For example, the recent drilling project at the Bosumtwi impact structures in Ghana revealed magnetic properties of rocks beneath the crater floor [Elbra et al., 2007]. Although a previous magnetic modeling had predicted presence of highly magnetized body, such material was not recovered.

Detailed intensity distributions of remanent magnetization of the lunar [Halekas et al., 2002] and Martian [Acuña et al., 1999] surface were mapped using magnetic field data derived from satellite observations. One of the re-

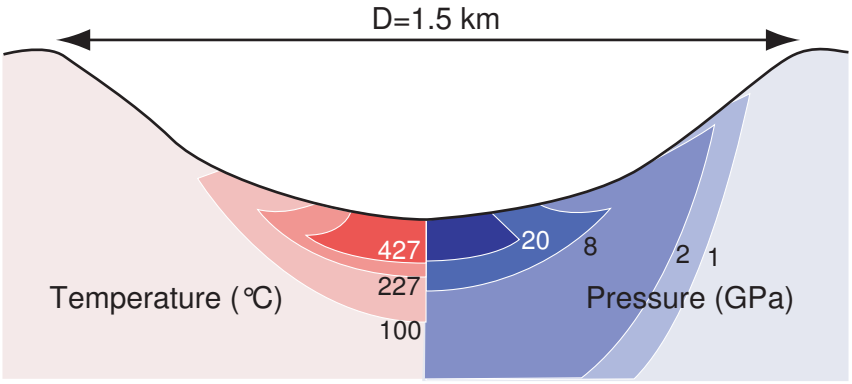

Figure 1.1: Maximum pressure (right) and temperature (left) calculated for a 1.5 km diameter impact crater formed in granite, modified after Ugalde et al. [2005].

markable features was demagnetized areas around impact craters or basins. The demagnetized area extend to 2−4 crater radii on the moon [Halekas et al., 2002] and 1.4 radii on Mars [Mohit and Arkani-Hamed, 2004]. The magnetic lows inside the structures was interpreted as results of thermal demagnetization of crustal rocks; i.e., post-shock temperature increase and subsequent cooling in absence of external field. However, thermal demagnetization could not explain the magnetic lows at outside the crater rim. Shock demagnetization was suggested as the cause, referring to the results of laboratory impact experiments described below.

1.2 Review of previous shock experiments

Before reviewing earlier shock experiments, shock pressure and temperature involved in cratering process should be mentioned. A hypervelocity impact of projectile generates shock waves in both the projectile and the target. The shock wave essentially decays concentrically in the target. By the shock compression, the target is heated to a certain post-shock temperature, which increases with increasing shock pressure. The most of the projectile and the target near the impact is largely transformed to melt and vapor (>50 GPa). Beyond the regions where the target is vaporized and melted, target material will be shock metamorphosed (>5 Gpa) or fractured. Many of the vaporized, molten, and shock-metamorphosed materials are ejected from the transient cavity. Some of the ejected materials fall back to the ground. Fig. 1.1 illus-

trates estimated peak pressures and temperatures around final crater with a diameter of 1.5 formed in granite.

In many of previous shock experiments, igneous rocks containing titanomagnetite with variable Ti content were used as targets. Shock pressures were produced using various techniques: impact of high-velocity projectiles [Hargraves and Perkins, 1969; Pohl et al., 1975; Cisowski and Fuller, 1978], explosives [Pesonen et al., 1997; Gattacceca et al., 2007], or laser [Gattacceca et al., 2006]. Although the peak shock pressures of the above experiments ranged from 0.25 to 35 GPa, some of the early studies [Hargraves and Perkins, 1969; Cisowski and Fuller, 1978] did not provide accurate estimates of the pressure.

The primary results of shock on magnetized igneous rocks are demagnetization of the primary remanence. With increasing shock pressures, larger intensity [Cisowski and Fuller, 1978] and higher-coercivity fraction [Pohl et al., 1975] of remanence is demagnetized. Significant portions of isothermal remanent magnetization (IRM) and thermal remanent magnetization (TRM) of basalt were demagnetized already at shock pressure of 0.25 GPa [Pohl et al., 1975] and IRM was completely demagnetized at 2 GPa [Gattacceca et al., 2006]. In contrast, NRM of basalt was unaffected at shock pressures below 7 GPa [Gattacceca et al., 2007], which indicate NRM is much more resistant to shock than IRM.

In the presence of external field, the shocked igneous rocks were also remagnetized parallel to the field direction [Pohl et al., 1975; Cisowski and Fuller, 1978]. This soft component is often referred to as shock remanent magnetization or SRM. The intensity of SRM in the pressure range of at least $0.25-1$ GPa is a function of shock pressure [Pohl et al., 1975]. Relationship between stability of SRM and shock pressure is unknown.

Low-field susceptibility is decreased and coercivity is increased by shock [Hargraves and Perkins, 1969; Pesonen et al., 1997; Gattacceca et al., 2007]. Degrees of these changes for diabase samples containing Ti-poor titanomagnetite were increased with increasing pressure up to 35 GPa [Pesonen et al., 1997]. Similar changes were induced in basalt containing Ti-rich titanomagnetite at shock pressures above 7 GPa [Gattacceca et al., 2007]. Decrease in magnetic susceptibility was also observed for granodiorite at a nuclear test site [Hargraves and Perkins, 1969].

Gattacceca et al. [2007] demonstrated that explosive-driven shocks of about 10 GPa on basalt and microdiorite acted to change their anisotropy of low-field magnetic susceptibility (AMS) as shown in Fig. 1.2. The degree of AMS was

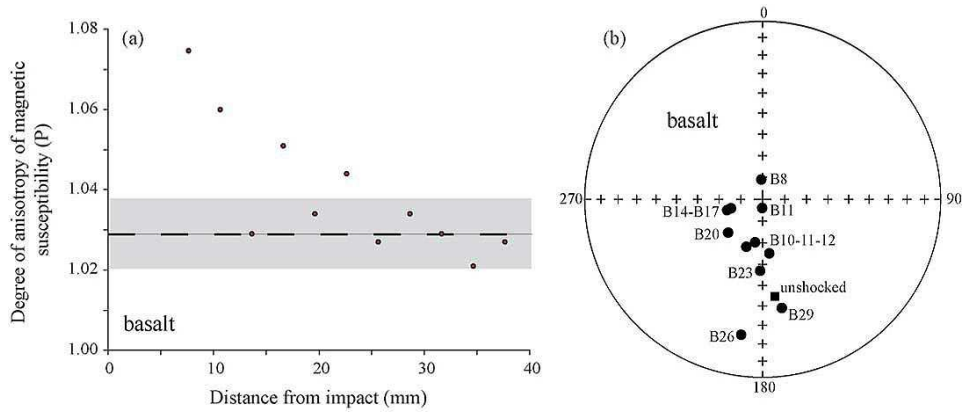

Figure 1.2: Effect of explosive-driven shock on AMS of basalt [Gattacceca et al., 2007]. (a) Degree of anisotropy of magnetic susceptibility vs. distance to the explosion. Pre-shock average is indicated by dashed line with one standard deviation (grey bands). (b) Lower-hemisphere equal area projection of minimum principal axis (K_3). The sample numbers correspond to the depth in mm.

increased near the shock surface, and the minimum principal susceptibilities were reoriented toward the shock direction. The AMS of terrestrial rock is usually controlled by the preferred orientation of magnetic minerals related to the primary formation of the rock or later tectonic deformation. The result of the experiment indicates that meteorite or rocks from impact craters might not exhibit the primary AMS.

1.3 Lonar impact crater

Lonar crater is located in central India (19°59'N, 76°31'E) as shown in Fig 1.3). The crater is nearly circular and has a rim-to-rim diameter of 1.8 km (Fig. 1.4 and Fig. 1.5). The formation age was estimated to 50,000 years ago or earlier [Storzer and Koeberl, 2004]. We believe that Lonar crater has several features that make the crater significant to study shock effects on rock magnetic properties: (1) good surface exposure of the basalt flows in the crater wall; (2) minimum alteration of basalt since the formation of the crater; (3) presence of extensive paleomagnetic studies of Deccan Traps, which provide information on magnetic properties and NRM components of unshocked basalts; (4) a closer analogy to the impact structures on basaltic crust on Mars.

Earlier studies [Cisowski and Fuller, 1978; Poornachandra Rao and Bhalla,

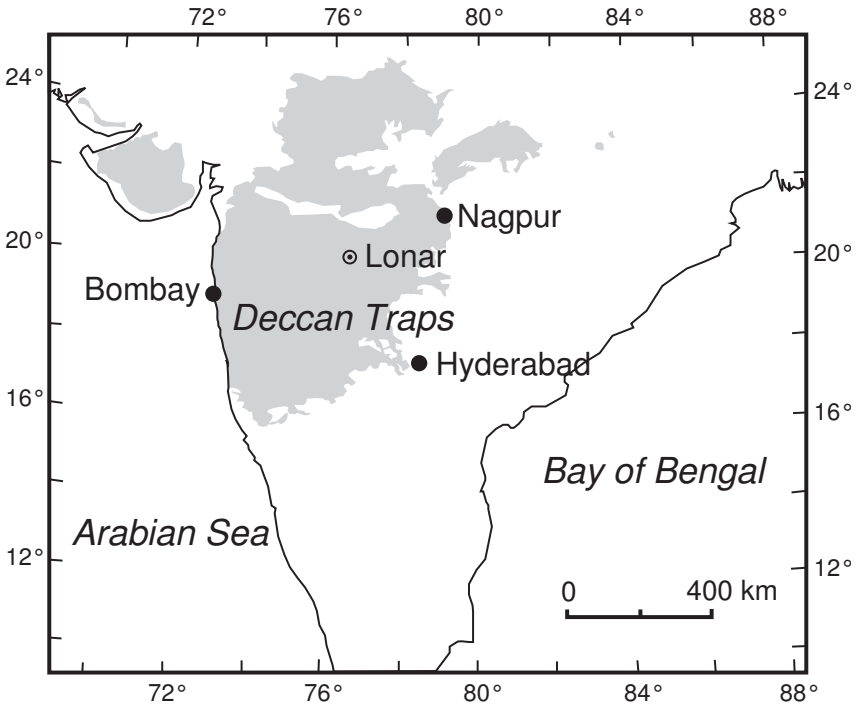

Figure 1.3: Map of India showing the location of Lonar. Deccan Traps are indicated by shaded area (Modified after Mahoney [1988]).

1984] isolated two NRM components from the basalts flows in the crater wall. The stable NRM component is likely the primary remanence of Deccan basalts, while the soft NRM component is oriented close to the present earth field direction. Poornachandra Rao and Bhalla [1984] reported that the NRM intensity is decreased toward the crater center and soft NRM component is larger in the lower flows. Based on these observations and the results of the shock experiments mentioned above, they suggested shock demagnetization and remagnetization of Lonar basalts; i.e., More reduced NRM near the crater center is due to stronger shock pressures, and SRM was acquired preferentially in the lower flows due to the relative abundance of low-coercivity grain. Lonar basalt exhibits high Königsberger ratio (>1.0). If the suggestions (shock de/remagnetization) would be correct, magnetic anomalies that extending out of the crater rim would be observed in a future study. This possibly explains the magnetic anomalies of impact structures on the moon or on Mars described above.

Figure 1.4: Satellite image of Lonar crater.

Figure 1.5: Panoramic view of Lonar crater from the eastern rim.

1.4 Identification of SRM

The fold test of overturned or tilted strata in the crater wall may be a unique method to detect SRM [Cisowski and Fuller, 1978]. The impacting meteorite penetrates the target rocks and releases its kinetic energy, generates shock waves (Fig. 1.6). The shock wave in the target expands downward and laterally, and weakens as it expands. The shock wave is detached because the rarefaction from the rear of the projectile encroaches [Melosh, 1989]. SRM is supposedly acquired simultaneously at the release from the shock pressure. After the passage of the shock and rarefaction waves, a residual particle velocity is imparted to the material, which marks the beginning of the excavation flow. The initial uplifting of the crater rim is continuation of the processes that excavated the crater. Therefore fold test should be positive if the low-coercivity component is related to shock.

There are a few possible explanations that the tilted strata did not gravitationally collapse to the pre-impact horizontal positions. Kumar [2005] observed various types of impact-induced fractures in the upper wall of Lonar crater. These fractures may cause bulking of the flow sequence below the crater rim [Collins et al., 2004]. In addition to the in-situ brecciation, deep drilling at the rim of Meteor Crater in Arizona demonstrated that the fragments of the target and meteorite are horizontally injected in the wall rocks. It is however not clear that such debris dikes are present beneath the rim of Lonar Crater.

The flows in the upper walls of Lonar crater are generally tilted outward, with the average dips of $10°-30°$. The dips are steepest near the rim, and become gentler as the distance from the rim is increased. Flow sequence of Deccan Traps is generally flat lying with dips of $1°$ or less [Mahoney, 1988]. Thus the tilting is obviously related to impact-induced structural uplifting. The average height of the present rim crest from the surrounding ground surface is 30 m, of which about 25 m is due to structural uplift and 5 m is due to upturned ejected debris [Fudali et al., 1980]. The exceptionally steep dipping ($50°-70°$) in the north-eastern wall was probably formed by slumping of the wall of the transient cavity during the crater modification stage [Kumar, 2005].

1.5 Purpose of the present study

Presence of possible giant impact crater(s) in Wilkes Land in East Antarctica was deduced from gravity data derived from the GRACE observations [von

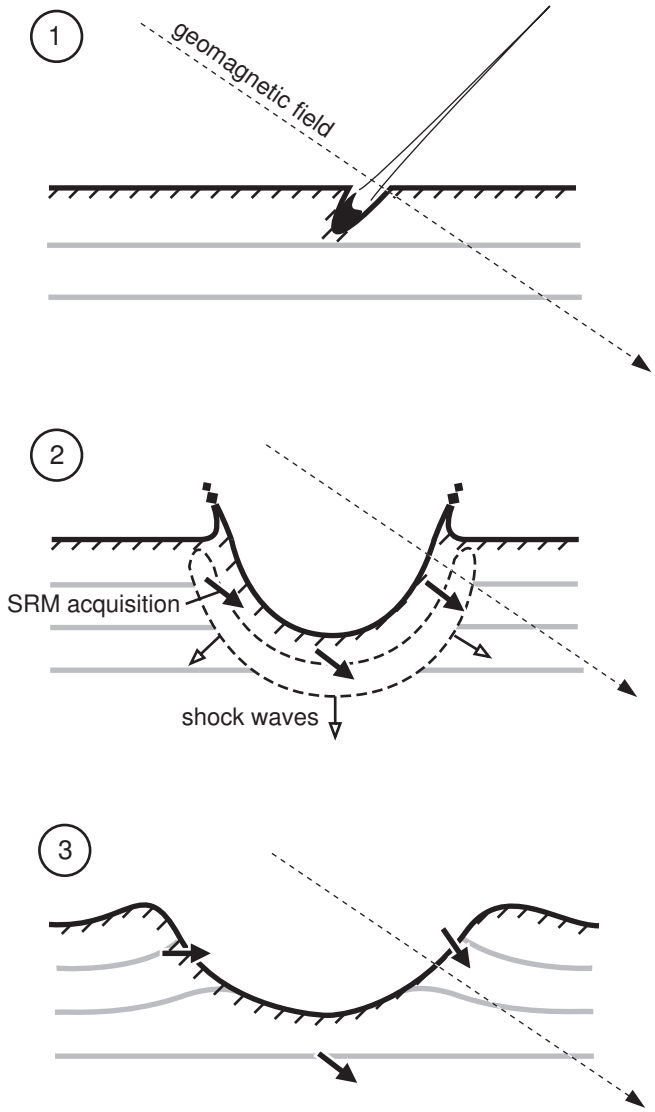

Figure 1.6: Schematic illustrations showing simple crater formation and acquisition of SRM (shock remanent magnetization).

Frese et al., 2006]. A circular positive anomaly found in this region is analogous to those at large impact basins on Mars. The sub-ice sheet topographic peak ring surrounding the anomaly has a diameter of approximately 500 km, which is larger than the diameter of Chicxulub Crater (∼180 km) in the Yucatan Peninsula formed at the Cretaceous-Tertiary boundary. Multiple impacts in wide area of Wilkes Land were also suggested based on the presence of multiple ring-shaped structures in aeromagnetic and satellite gravity data [Weihaupt and Rice, 2007]. Confirmation of the impact origin is critical from the aspects of biological evolution on earth, as impact of large meteorites should impact on the global environment.

In order to correctly interpret the magnetic data, it is required to have a basic concept of how shock affects magnetic properties of surrounding rocks. Several studies revealed possible shock effects on magnetic properties of highly shocked materials in central part of crater, e.g., shock remanence [Halls, 1979], demagnetization [Robertson and Roy, 1979], and random orientation of NRM vector [Carporzen et al., 2005]. In contrast, magnetic properties of less shocked material in crater wall remains poorly studied, probably in part due to limited exposure of rocks at many terrestrial impact craters. However, as already mentioned, the magnetic anomaly maps of the lunar and Martian surface indicate probable shock effects on rocks even beyond crater rims.

This thesis investigates effects of relatively weak shock on various magnetic properties through laboratory shock experiments and study of Lonar impact crater. Gattacceca et al. [2007] described the changes in magnetic properties of various types of rocks due to decaying stress waves with the initial peak pressures of 30 GPa. The pressure estimate is, however, less secure in the lower pressure range (<5 GPa), which is expected for the material in the crater wall. Thus we first describe shock effects on several magnetic properties in this pressure range. Magnetic properties of basalts in the crater wall of Lonar crater are then described.

The main body of this thesis is composed of three parts found in Chapter 2, 3, and 4. Chapter 2 describes the result of the shock experiment. Initial shock pressure of 5 GPa was generated in a basaltic andesite block; The effects of the decaying stress waves on NRM, low-field magnetic susceptibility, hysteresis, and AMS were subsequently measured. The present study aimed to describe changes in magnetic properties with more accurate pressure estimate. Chapter 3 and 4 mainly describe the results of magnetic study of basalt from Lonar impact crater in India. In Chapter 3, magnetic mineralogy, hysteresis

properties, and AMS are studied for the target rocks in the crater rim. In Chapter 4, shock effects on NRM were evaluate via tilt correction of the flows in the crater wall and detailed investigation of magnetic properties.

Chapter 2

Shock experiment on basaltic andesite: Irreversible changes in magnetic properties

2.1 Experiments

Stress waves were produced in the rock target using a single-stage propellant gun (30 mm bore) housed at the National Institute for Materials Science, Japan. The target was a cubic block of basaltic andesite ($17 \times 17 \times 17$ cm) housed in a stainless steel (SUS 304) container (Fig. 2.1). The target was further covered by silicon steel plates; The measured field intensity on the impact surface was 0.002 mT. A cylindrical aluminum projectile with a diameter of 11.75 mm and length of 38 mm (weight, 46.0 g) was set on a high-density polyethylene sabot. The projectile was accelerated to an impact velocity of 0.725 ± 0.25 km/s to produce an initial pressure of 5.2 ± 0.2 GPa, as determined using the impedance match method. We used the Hugoniot data for aluminum in Marsh [1980] and that for basalt in Nakazawa et al. [1997]. The duration of such a compression is considered to be in the order of microseconds [Nakazawa et al., 2002]. The projectile impacted near the center of the target surface. The target remained intact except for the formation of a shallow surface crater (3 cm diameter and 2 mm depth) as shown in Fig. 2.2. We observed many tensile cracks parallel to the impacted surface in the regions between the crater floor and a depth of 3 mm (Fig. 2.3). Subvertical cracks and local fractures were observed at deeper levels within the target.

We prepared 14 continuous cubic specimens ($6 \times 6 \times 6$ mm) from directly

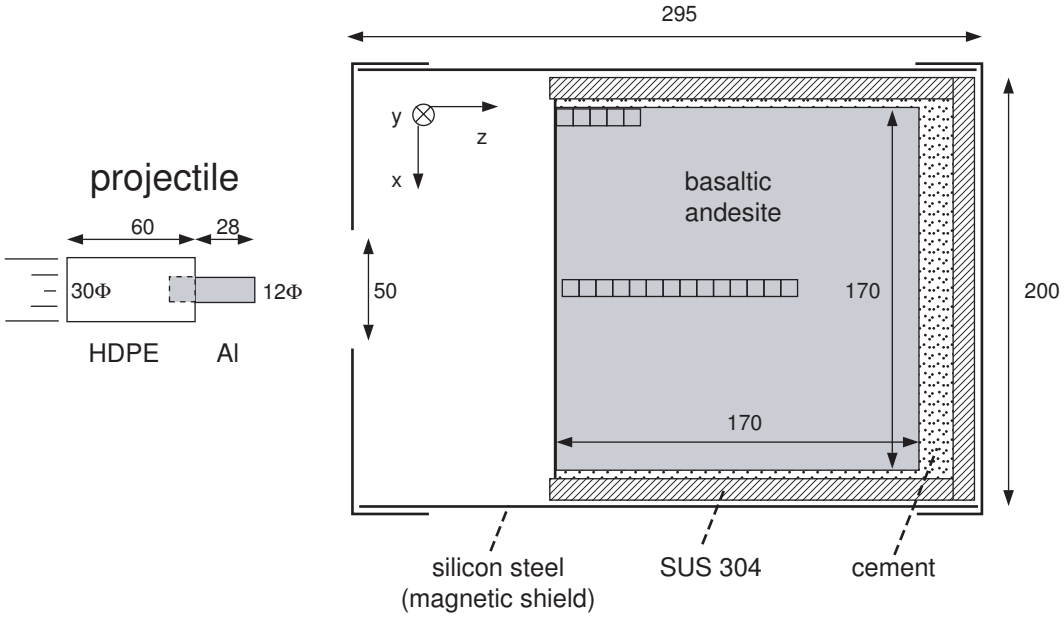

Figure 2.1: Schematic views of the projectile and the target.

beneath the center of the crater floor; i.e. down to a depth of about 10 cm (Fig. 2.1). The specimens were numbered i01, i02, i03, etc., starting at the uppermost specimen. Five control specimens of the same size, which we assumed to be less shocked than the specimens from the central area, were cut from the side part of the target block (at 8 cm distance from the crater center, in the region near the impact surface). Pressure decay beneath the impact point was estimated after Nakazawa et al. [2002], whose planar shock experiments on basalts revealed that the relationship between the measured peak pressure, P_s, and the distance beneath the impact surface, x, can be formulated as follows:

$$P_s/P_0 = \begin{cases} 1 & (x \leq r), \\ (x/r)^{-1.7} & (x > r). \end{cases}$$

where P_0 is the initial pressure and r is the projectile radius. These equations were used in the present study to obtain estimates of the pressure ranges for each specimen (Fig. 2.4).

AMS was measured at room temperature (25°C) using an AGICO KLY-3S Kappabridge. The operating frequency and field intensity were 875 Hz and 0.4 mT, respectively. AMS was measured before and after two-axis tumbling alternating field demagnetization (AFD) in a peak field of 80 mT. The average low-field susceptibility, K_m, was calculated as $K_m = (K_1 + K_2 + K_3)/3$, where

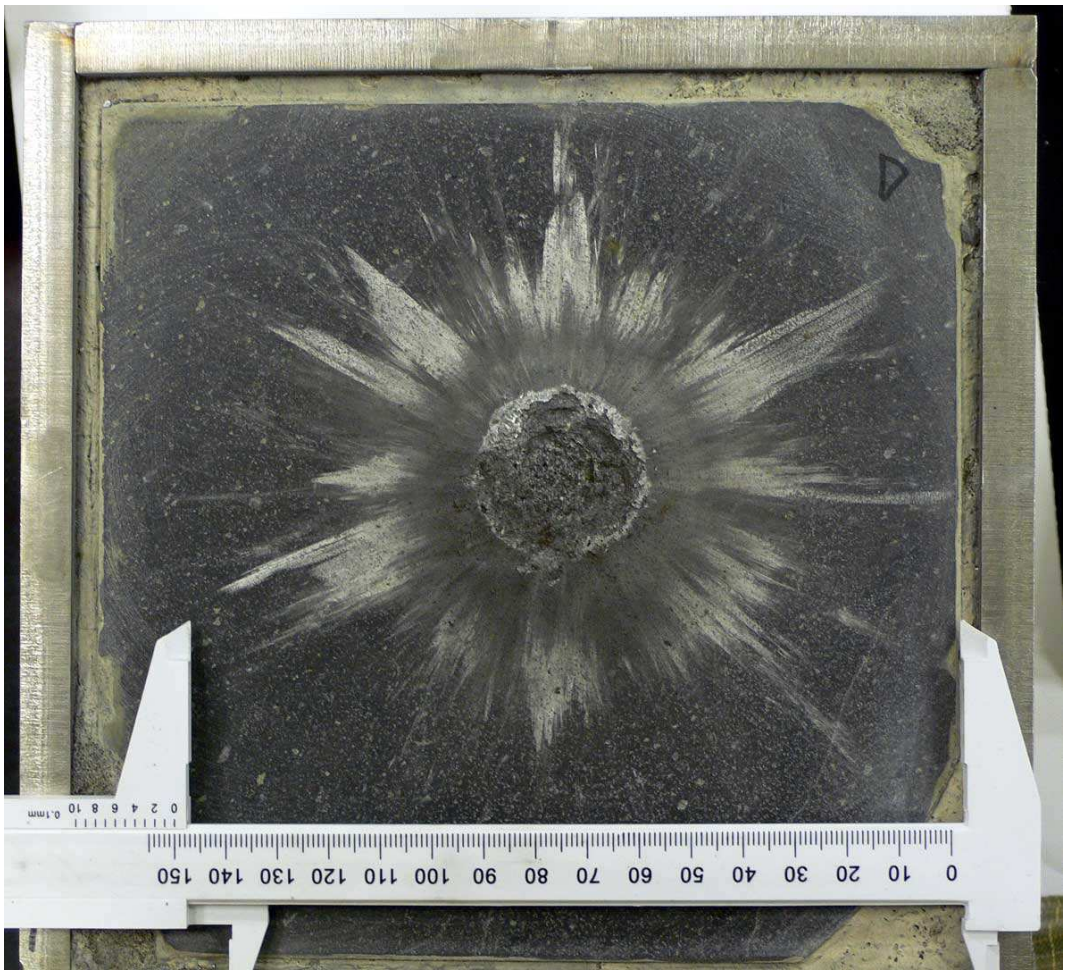

Figure 2.2: Impact crater formed on the surface of the basaltic andesite target.

Figure 2.3: Reflected-light micrograph of specimen i01. The upper base is the crater floor. The homogeneous gray areas in the upper half of the specimen are epoxy-filled cracks.

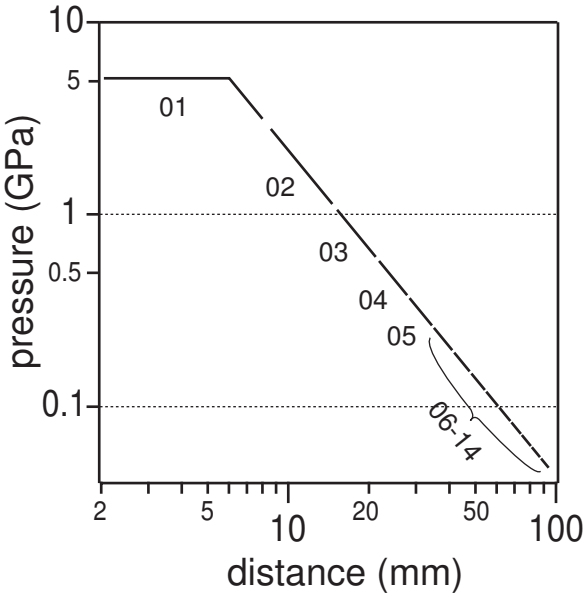

Figure 2.4: Pressure decay beneath the impact point as a function of distance from the surface (see text for equations).

K_1, K_2, and K_3 are the principal susceptibilities ($K_1 \geq K_2 \geq K_3$). The shapes of the AMS ellipsoids were characterized in terms of a shape parameter, T, and anisotropy degrees, P', after Jelinek [1981].

$$\begin{aligned} T &= (2\eta_2 - \eta_1 - \eta_3)/(\eta_1 - \eta_3) \\ P' &= exp\sqrt{2[(\eta_1 - \eta_m)^2 + (\eta_2 - \eta_m)^2 + (\eta_3 - \eta_m)^2]} \end{aligned}$$

where

$$\eta_1 = lnK_1, \eta_2 = lnK_2, \eta_3 = lnK_3, \eta_m = (\eta_1 + \eta_2 + \eta_3)/3$$

We also measured hysteresis curves of the same specimens at room temperature with a maximum field of 1.0 T and using a vibrating sample magnetometer (Riken Denshi, BHV-50). The average hysteresis parameters for each specimen were calculated as $(A_p + 2 \times A_n)/3$, where A_p and A_n are the hysteresis parameters measured parallel and perpendicular to the shock direction, respectively.

Table 2.1: Magnetic hysteresis parameters of basaltic andesite from Mt. Omuro at room temperature.

H_c (mT)	H_{cr} (mT)	I_s (Am^2/kg)	I_r (Am^2/kg)	K_p (m^3/kg)
9.5	21.0	0.50	0.12	2.29E-07

Notes: Coercivity, H_c; remanence coercivity, H_{cr}; saturation magnetization, I_s; saturation remanence, I_r; and high-field magnetic susceptibility, K_p.

2.2 Initial mineralogy and magnetic properties

The target rock was sampled from Quaternary lava flows at Mt. Omuro, Izu Peninsula, Central Japan. The bulk density of the basaltic andesite, as measured from a cylindrical core, was 2.74 g/cm^3. This value is similar to those (2.63 to 2.74 g/cm^3) recorded for basalts used in previous shock attenuation experiments [Nakazawa et al., 2002]. The petrology and mineralogy of Omuro basaltic andesite was described in Hamuro [1985]. The sample contains phenocrysts of olivine and plagioclase in a groundmass of plagioclase, augite, orthopyroxene, pigeonite, and titanomagnetite.

A reversible thermomagnetic curve in a vacuum ($\sim 10^{-3}$ Pa) up to 600°C was obtained using the vibrating sample magnetometer (Fig. 2.5). A single Curie point at 180°C indicates presence of $Fe_{2.4}Ti_{0.6}O_4$ or TM60 [Akimoto et al., 1957]. Magnetic hysteresis parameters at room temperature after slope correction are shown in Table 2.1. Titanomagnetite content was estimated to be 1.1 vol.% based on a saturation magnetization (I_s) of 125 kA/m expected for stoichiometric TM60 [Dunlop and Özdemir, 1997]. A comparison of obtained ratios of saturation magnetization to saturation remanence (I_s/I_r) and remanence coercivity to coercivity (H_{cr}/H_c) with data presented by Day et al. [1977] indicates that the present values correspond to a grain size of 3 to 6 μm of crushed TM60. Under the optical microscope, titanomagnetite grains are observed to be 20 μm in size or smaller. The average ferromagnetic contribution to low-field susceptibility (C_f) was determined to be 96% using the following equation:

$$C_f = (K_m - K_p)/K_m$$

where K_p is high-field susceptibility calculated from the slope between 0.7 and

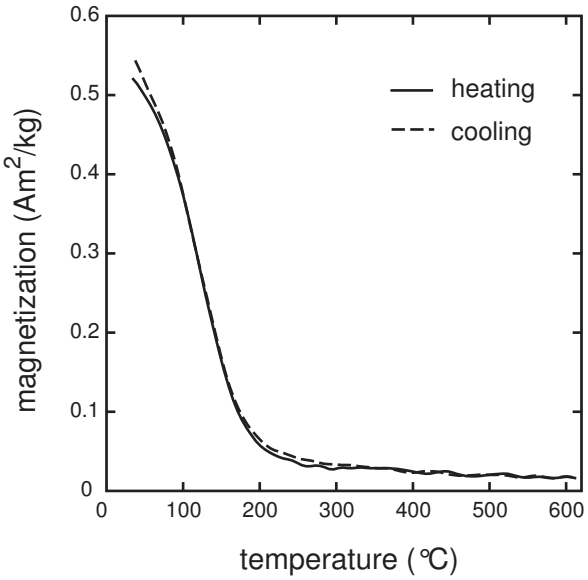

Figure 2.5: Thermomagnetic curve in vacuum.

1.0 T in the hysteresis loop.

2.3 Shock effects on magnetic properties

2.3.1 Hysteresis parameters and NRM

The target between the depths of 10 and 100 mm showed no systematic change in K_m (Fig. 2.6, upper); the average value and standard deviation was 5.97 $\pm$ 0.14 ($\times 10^{-6}$ m^3/kg), similar to the values obtained for the side specimens (not shown; $5.95 \pm 0.11 \times 10^{-6}$ m^3/kg). K_m was reduced by about 30% in areas close to the impact (i01) relative to areas in the lower part of the specimen. In contrast, saturation magnetization, I_s, was unaffected by the impact. The average I_s value of the beneath-crater specimens was 0.49 ± 0.02 Am^2/kg. The patterns of variations in K_m and I_s are similar among the lower specimens. Therefore, the K_m values of specimens i02 to i14 did not show a significant decrease: their minor variations reflect heterogeneity in the volume density of magnetic grains. The decrease in K_m recorded for the uppermost specimen (i01) was associated with the impact.

Coercivity, H_c, and the coercivity of remanence, H_{cr}, are generally constant for the lower specimens between i05 and i14, with average values of 9.0 and 19.5 mT, respectively (Fig. 2.6, middle). These parameters increased by

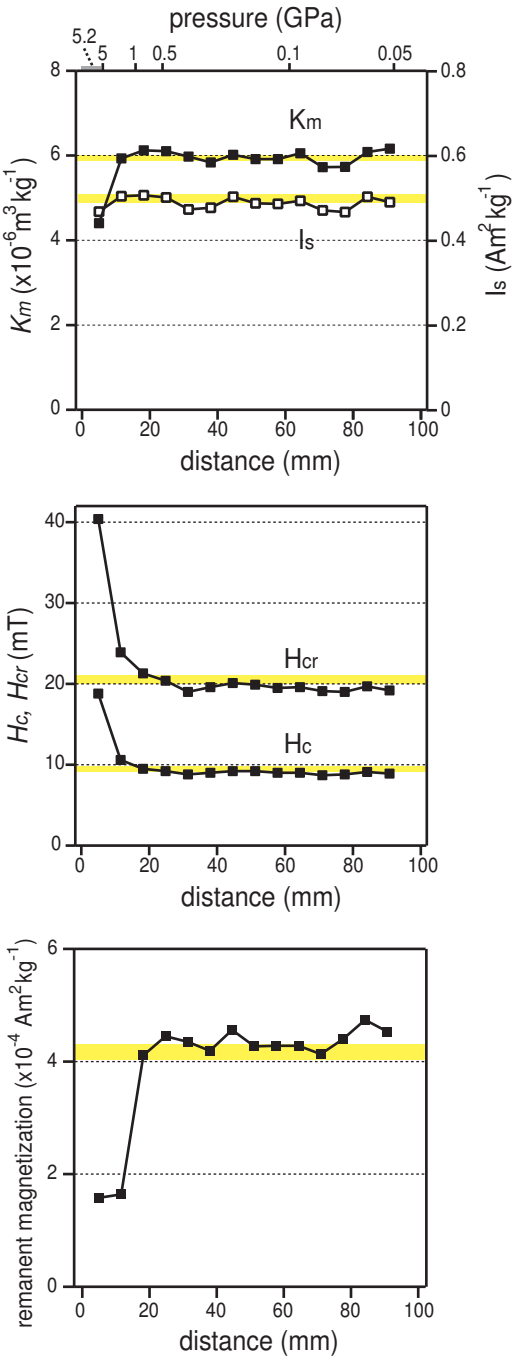

Figure 2.6: Post-impact magnetic parameters of the target rock as a function of the distance from the impacted surface toward the center of the specimen. Low-field magnetic susceptibility, K_m; saturation magnetization, I_s; coercivity, H_c; and remanence coercivity, H_{cr}; natural remanent magnetizaiton, NRM. Yellow bands indicate one standard deviation uncertainty for five specimens from the side of the block.

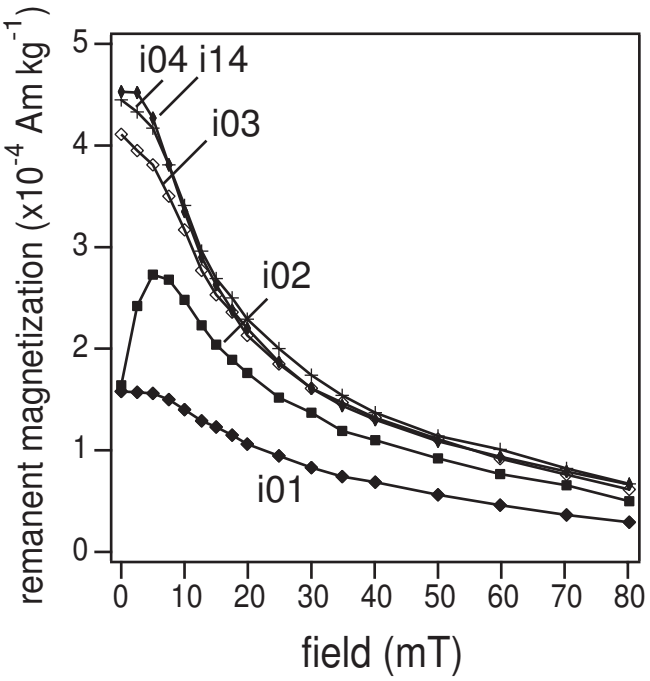

Figure 2.7: Alternating field demagnetization of specimens i01, i02, i03, i04, and i14.

approximately 100% for specimen i01, and to a lesser extent for specimen i02 and possibly i03.

The primary NRMs of samples between i03 and i14 appear to have been unchanged by the impact, while those of i01 and i02 were partially demagnetized (Fig. 2.6, lower). The increase of NRM for i02 after AFD (5 mT) is due to removal of soft component, which is likely shock-related remanence. In contrast, NRM intensity of i01 was unchanged after AFD (5 mT); i.e. no SRM was acquired and the primary low coercivity remanence was completely shock-demagnetized.

2.3.2 Coercivity spectra of the residual NRM

NRM of a wide range of coercivity were demagnetized by the impact (Fig. 2.7). The decay curves of specimens i01 and i02 remained lower than those of the less shocked specimens even after the demagnetization at a peak field of 80 mT. However, demagnetization appears especially significant in the low-coercivity range (0-10 mT). The decay curve of specimen i01 was flattened in this field range due to complete demagnetization of the initial NRM. Demagnetization of the low coercivity fraction is also indicated for specimen i03.

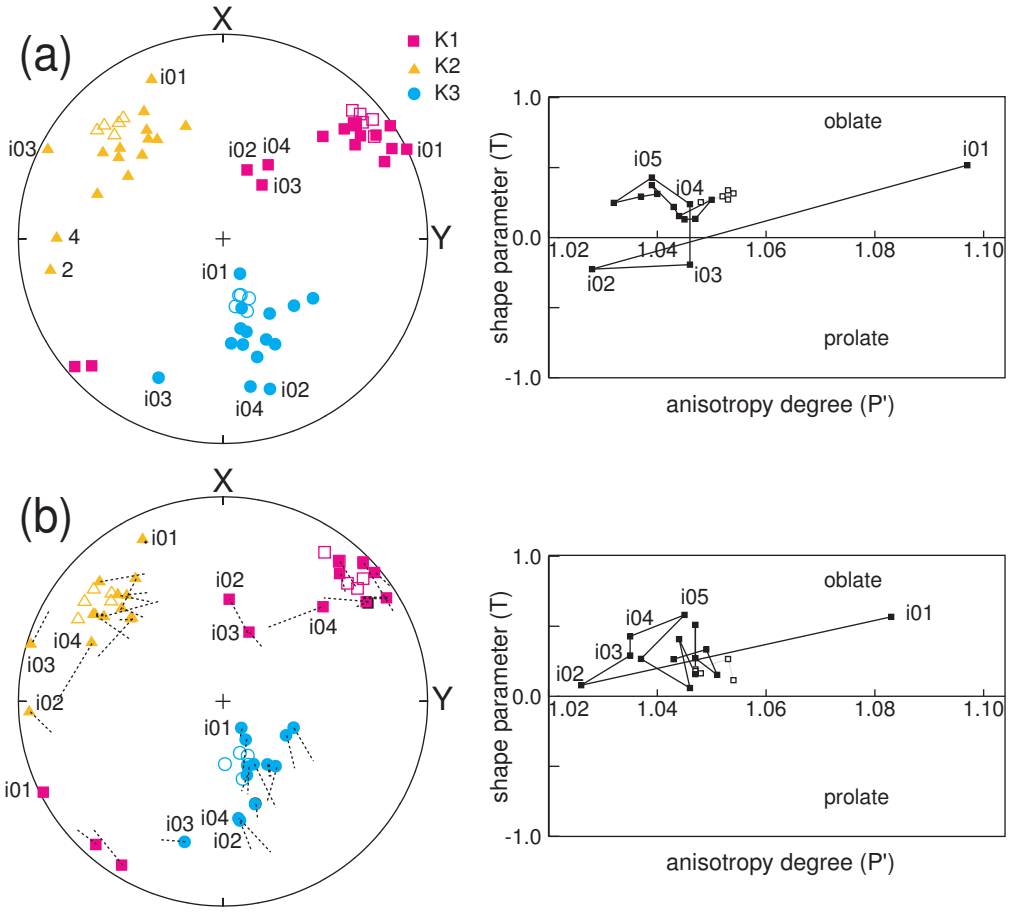

Figure 2.8: AMS parameters of the target rock (a) before and (b) after tumbling AFD with a peak field of 80 mT. The solid and open symbols denote data from specimens located beneath the impact point and from the side of the target block, respectively. Left: Lower-hemisphere equal-area projection showing the orientations of the principal susceptibility axes. The vertical is the shock direction. Numbers denote specimen ID. The trajectories of the principal susceptibility axes before and after AFD are also shown. Right: plot showing the shape of the AMS ellipsoids. Anisotropy degree, P', and shape parameter, T, are after Jelinek [1981].

2.3.3 Anisotropy of magnetic susceptibility

The orientations of the principal susceptibility axes are shown in Fig. 2.8 (left). Those of the side specimens show tightly clustered triaxial distributions, but the specimens from beneath the impact point show a wider distribution. The inclinations of the minimum axes of specimens from beneath the impact point are generally shallower than the primary directions. The changes are most remarkable for specimens located close to the impact (i02 to i04), for which the easy (K_1) axes are subparallel to the shock direction. In contrast, specimen i01 has the K_3 axis oriented close to the shock direction. Figure 2.8a (right) reveals that the AMS of the side and lower specimens shows slightly oblate (T>1) AMS ellipsoids, with P' values of about 1.05. The side specimens record only minor variations in the AMS shape parameters. The AMS ellipsoids show a gradual change in shape with increasing pressure. The shifts in the data points are more pronounced close to the impact point (i01 to i05), and specimen i01 records a high P' value. These results indicate that the observed changes in the shape, degree, and orientation of the AMS ellipsoids occur at lower pressure relative to that leading to a reduction in K_m.

The principal susceptibility axes of the side specimens showed no significant change in orientation or shape of AMS ellipsoids following AFD (2.8b); in contrast, the specimens sampled from directly beneath the impact showed a general change in their AMS parameters. The average orientations of the principal axes of the samples from directly beneath the impact changed to orientations similar to those of the side specimens. The lower specimens showed no significant changes in T and P' following AFD; however, remarkable shape changes were observed for specimens sampled from close to the impact.

2.4 Discussion

Increase in coercivity and decrease in low-field susceptibility was observed for the target just beneath the impact. Similar phenomenon was previously reported for uniaxially compressed magnetite-bearing sandstones [Jackson et al., 1993]. The above observations can be interpreted as magnetostrictive effect of titanomagnetite caused by increased internal stresses [Syono, 1965]. Reduction in effective grain size of titanomagnetite is probably insignificant as a cause of the observed features, because susceptibility is probably a grain size independent parameter [Heider et al., 1996]. The results of the present exper-

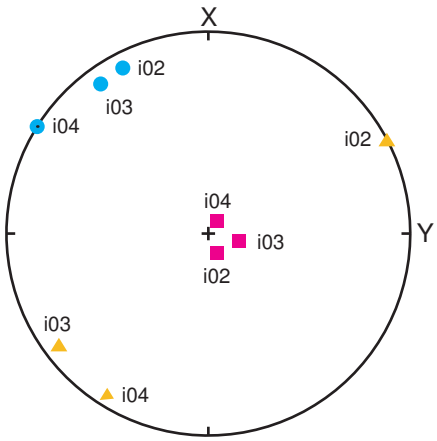

Figure 2.9: A lower-hemisphere equal-area projection showing the orientations of the principal susceptibility axes for specimens i02 to i04, after isolation of the shock-induced component. Symbols are the same as those for Fig. 3 (left).

iment also showed that shock changes the initial coercivity more sensitively than susceptibility. This is probably because coercivity, unlike susceptibility, is related to irreversible magnetization processes [Heider et al., 1996]; i.e., the pinning and unpinning of domain walls at lattice defects.

The observed AMS changes can be classified into the following three levels: (1) low shock pressure of less than 0.4 GPa (specimens i05 to i14) that induced only minor changes in the directions and shapes of the AMS ellipsoids; the shock effects were removed by tumbling AFD; (2) intermediate shock pressure ranging from 0.4 to 3 GPa (i02 to i04) that produced K_1 axes oriented subparallel to the shock direction; tumbling AFD partly remove this effect; and (3) high shock pressure of greater than 3 GPa (i01) that gave rise to a significant increase in P' and decrease in K_m; the K_3 axis changed from the initial direction to the shock direction, and the new AMS was highly stable against AFD. Gattacceca et al. [2007] observed similar changes in AMS for basalt and microdiorite shocked to pressure greater than 10 GPa.

The changes observed at low to intermediate shock pressures are generally similar to those reported from experiments involving static loading. Kapicka [1988] reported that the elastic deformation of basalt arising from uniaxial stresses up to 60 MPa caused essentially reversible changes in AMS. This result indicates that the magnetic domains are ordered when subjected to the external stress, but revert to the initial configuration with release of the stress [Appel and Soffel, 1985]; however, small irreversible changes in AMS do

occur [Kapicka, 1983], probably related to pinning of domain walls at lattice defects or the irreversible rotation of spontaneous magnetization to other easy axes. Such stress-induced anisotropy has been suggested to be removable by tumbling alternating field demagnetization [Park et al., 1988]. In contrast, the AMS changes recorded at intermediate to high shock pressures may be related to either the fracturing of magnetic grains Gattacceca et al. [2007] or the formation of lattice defects such as dislocations. The both mechanisms are consistent with the high stability of the AMS changes against AFD (2.8b). We confirmed via optical microscopy that grain rotation is not responsible for the AMS changes.

The lack of exact parallelism between the K_1 axes and the shock direction for the intermediate-pressure specimens can be explained by the effect of the primary AMS. We introduce a simple model in which the measured AMS (F_1) represents the superposition of primary (F_0) and shock-induced (F_s) AMS, each represented as second-rank symmetric tensors. In this case, F_s is easily determined by subtracting F_0 from F_1. We used the average tensor of the five side specimens as F_0. Figure 2.9 shows that specimens i02 to i04 exhibit enhanced parallelism of the K_1 axes after isolation of the shock components. We do not presently have a theoretical model to explain the K_1 axes oriented parallel to the shock direction.

2.5 Conclusions

Irreversible changes in magnetic properties by stress waves were studied for basaltic andesite containing Ti-rich titanomagnetite. The result can be summarized as follows.

(1) AMS was induced in the pressure range higher than 0.4 GPa. The shock-induced AMS has K_1 axis coaxial to the shock direction at 0.4-3 GPa. In contrast, K_3 axis was reoriented toward the shock direction at 3-5 GPa. The anisotropy degree was significantly increased at 3-5 GPa.

(2) Coercivity was increased and susceptibility was decreased at 3-5 GPa. These changes are probably attributed to increased residual stress in titanomagnetite.

(3) Natural remanent magnetization (NRM) was partly demagnetized and remagnetized at 1-5 GPa. The low-coercivity fraction of NRM (< 5

mT) was completely demagnetized or remagnetized, and high-coercivity fraction (10-80 mT) was partly demagnetized. Approximately 35% of the initial NRM survived at 3-5 GPa.

Chapter 3

AMS of basalts from upper wall of Lonar crater

3.1 Geological setting

Lonar is located in the Buldana District of Maharastra State in India (19°59'N, 76°31'E as shown in Fig 1.3). Lonar crater is a circular, bowl shaped depression with a rim-to-rim diameter of 1.8 km. The average elevation of the rim crest is about 590 m, whereas that of the floor level is 470 m. The crater floor is occupied with shallow saline lake. The previous drillings through the crater floor revealed the presence of brecciated and pulverized basalt, overlain by post-impact sediment with maximum thickness of about 100 m [Fredriksson et al., 1973].

Findings of maskelynite [Fredriksson et al., 1973], shutter cones [Fredriksson et al., 1973], tektite like bodies [Murali et al., 1987], and molten rocks [Osae et al., 2005] confirmed the impact origin of Lonar crater. However, type of impactor that formed the crater is unknown. Lonar is one of the youngest terrestrial impact craters along with Meteor Crater in Arizona; Formation age of Lonar has been estimated between 15 and 53 ka [Storzer and Koeberl, 2004, and references therein].

As already mentioned, the crater excavated the basalt flows of Deccan Traps. The main eruptions occurred around 65−67 Ma [Vandamme et al., 1991] during the passage of Indian continent over the Reunion Hotspot. The eruptive sources of basalts are believed to be located near the west coast, probably offshore of Bombay and the Cambay area [Mahoney, 1988]. The thickness of the flow sequence in the Lonar area is probably 400−700 m. It

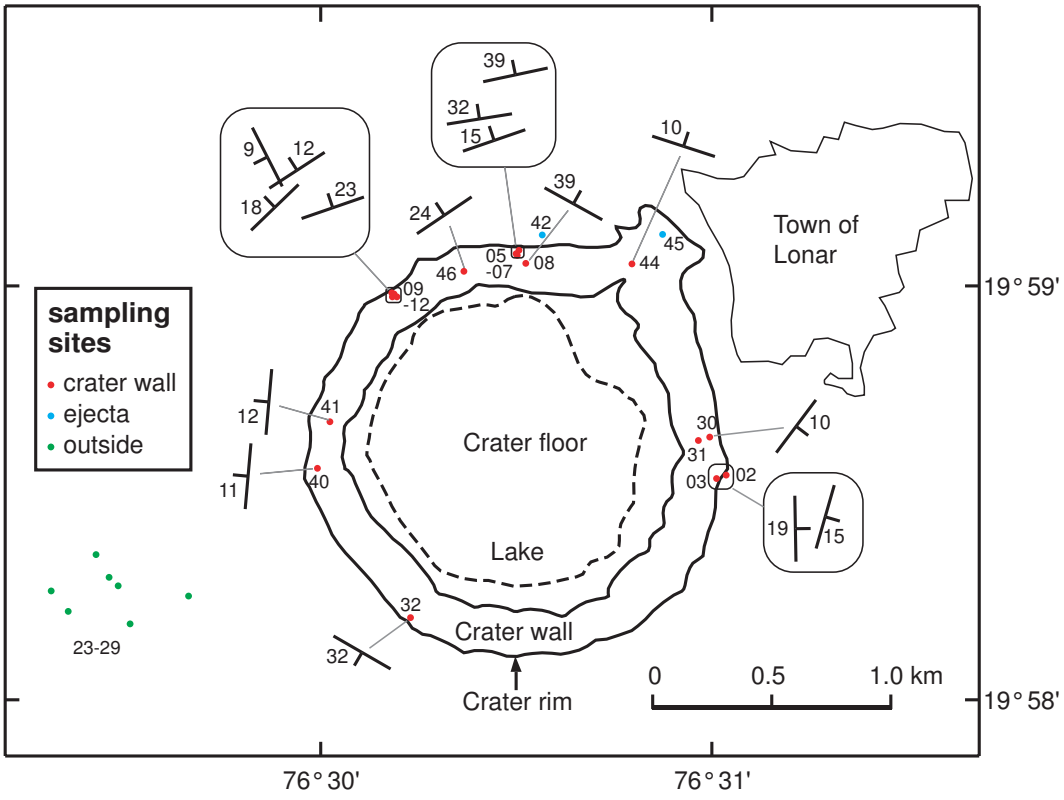

Figure 3.1: Map showing the location of the sampling sites with their site numbers, strikes, and dips.

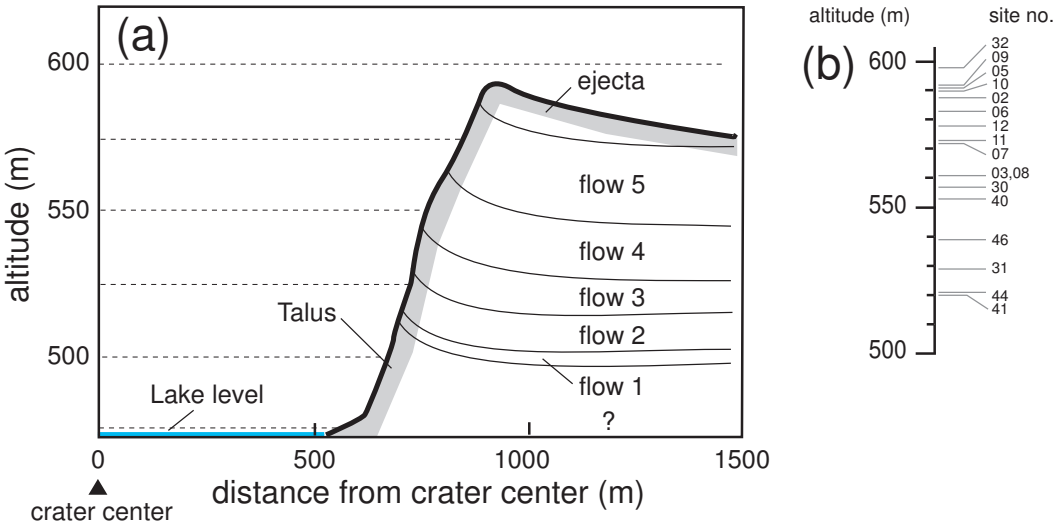

Figure 3.2: (a) Elevation profile and geology at the northern rim, modified after Maloof et al. [2005]. The vertical scale is exaggerated by a factor of seven. (b) Altitudes of the sampling sites on the crater wall.

is in debate if the impact excavated the underlying Precambrian basement [Chakrabarti and Basu, 2006]. Five tholeiitic pahoehoe flows are exposed on the innerwall of the crater (Fig. 3.2). The flows have the thickness ranging from 5 to 30 m, in which the uppermost flow is thickest. It is often difficult to identify the flows, due to covers of talus, soil, and vegetation. The different flows show very uniform whole chemical composition, with minor difference in abundance in phenocrysts [Kieffer et al., 1976].

3.2 Sampling

Basalts were sampled at total 26 sites: 17 sites in the crater wall, seven sites in the outside of the crater, and two sites in ejecta blanket (Fig. 3.2). Surface exposures of basalts in the crater wall are limited due to the cover of vegetation and talus. For the same reason, the flows were often difficult to identify. The altitude of the sampling sites in the crater wall ranged from 520 m to 600 m. We sampled the outside samples in the west of the crater, 0.7−1.3 km beyond the rim (at 1.8−2.4 radii). We sampled at six sites (sites 23−28) in wells of 5−10 m in depth and at a small horizontal exposure (site 29). The average altitudes of these seven sites are 546±2 m. The samples were collected from the uppermost flow (flow 5), probably the limited upper part of the flow. The

ejecta clasts were sampled in a pit at the northern rim and from a surface exposure located near the valley in the NNE rim. Less fractured lithic clasts of generally less than 1 m were sampled.

We sampled eight to eleven basalt cores at each sampling site using an engine-powered portable drill. Five and three block samples were collected at Site 32 and 46, respectively. One or two drill cores were later taken in a laboratory from each block samples at Site 32 and 46, respectively. Sampled core of 24 mm in diameter were cut into one or two specimens of 21 mm long. Weathered surface was avoided in the sample preparation. These drill cores or blocks were oriented in-situ with a magnetic compass. Local magnetic field deviation at Lonar Crater is $+1^\circ$ according to IGRF-10 model. The positions and altitudes of the sampling sites were determined using handheld global positioning system (GPS) receivers.

3.3 Experiments

AMS was measured at room temperature (25°C) using an AGICO KLY-3S Kappabridge (Brno, Czech Republic). The operating frequency and field intensity were 875 Hz and 0.4 mT, respectively. We measured AMS of one specimen from each core. The average low-field susceptibility, K_m, was calculated as $K_m = (K_1 + K_2 + K_3)/3$, where K_1, K_2, and K_3 are the principal susceptibilities ($K_1 \geq K_2 \geq K_3$). To characterize the AMS ellipsoids, we calculated degrees of anisotropy ($P = K_1/K_3$), lineation ($L = K_1/K_2$), and foliation ($F = K_2/K_3$). Orientations of the principal susceptibility axes were plotted after tilt correction.

Magnetic hysteresis at room temperature and temperature dependence of saturation magnetization (I_s) were measured using a vibrating sample magnetometer (Riken Denshi, BHV-50). These measurements were respectively performed for a large (about 2 g) and a small (0.05 g) specimen from each site. During the thermomagnetic runs, specimens were heated up to 610°C and cooled back to room temperature at a constant rate of 200°C/h, in vacuum (10^{-3} Pa), and in a direct field of 1 T. Temperature dependence of hysteresis properties were also studied for a limited number of specimens; Hysteresis loops were measured at steps of 20°C from room temperature to 620°C, and back to room temperature.

3.4 Results

3.4.1 Thermomagnetic curves

Study of temperature dependence of I_s showed nearly the same result as that presented in the previous study (Poornachandra Rao and Bhalla, 1984). The I_s changes were irreversible after heating up to 620°C; I_s at room temperature was increased by factors ranging from 0.9 and 1.6 (Table 3.1). Second heating runs showed reversible curves, indicating alteration of magnetic minerals in the first heating runs. The maximum Curie temperatures (T_c) ranged from 500° and 560°C. Unlike previously reported, we could not detect presence of titanohematite with T_c>600°C in the lower flow.

A typical example of temperature dependence of hysteresis properties is shown in Fig. 3.3. I_s (after subtracting paramagnetic contributions) was first dropped above 350°C during heating, and then completely lost at 540°C. I_s at room temperature was increased after heating, by a factor of 1.3 in this case. Low-field magnetic susceptibility (K_m) and coercivity (H_c) also showed respectively small drops or increase at 300°C although the similar change is absent in I_s. The same features in K_m and H_c appear in the cooling curves; However, the changes in K_m is smaller than those in the heating curve. The incrase in K_m above 350°C is consistent with the change observed for I_s.

3.4.2 Hysteresis parameters

The hysteresis parameters plotted on Day plot (Fig. 3.4) provides an estimation of average grain size of magnetite [Day et al., 1977]. All the data of Lonar basalts fall in the region of pseudo-single domain (PSD) size of magnetite. The most data fall just along the master curve of the single domain (SD) and multidomain (MD) mixing curves of magnetite [Dunlop, 2002]. This may justify the use of the plot as a magnetic granulometry indicator although it is not clear how low-temperature oxidation will affect to the hysteresis parameters.

3.4.3 The average susceptibility and shape of AMS ellipsoids

The AMS results of Lonar basalts showed predominantly foliated ellipsoids (F>L) as shown in Fig. 3.5a. The ratios of the foliated samples are 79% and 51% in the crater wall and outside flow sites, respectively. Three data points

Table 3.1: Site parameters and some magnetic properties.

Site No	altitude (m)	rim	strike (deg.)	dip (deg.)	Tc (°C)	Is_1/Is_0	K_m (10^{-5} m^3/kg)
outside							
23	545	SWW	-	-	530	1.52	1.61±0.34
24	543	SWW	-	-	560	1.08	1.14±0.05
25	550	SWW	-	-	530	1.31	1.39±0.20
26	546	SWW	-	-	560	1.18	1.02±0.04
27	546	SWW	-	-	470	1.09	1.57±0.24
28	546	SWW	-	-	510	1.47	1.04±0.05
29	546	SWW	-	-	555	1.42	1.11±0.09
innerwall							
02	587	E	16	15	565	0.92	1.28±0.44
03	561	E	359	19	530	1.15	1.48±0.26
05	591	N	258	39	560	1.43	1.14±0.17
06	583	N	261	32	525	1.11	0.99±0.05
07	572	N	251	15	530	1.64	1.07±0.07
08	561	N	299	39	560	1.18	1.65±0.10
09	592	NE	153	9	550	0.98	1.13±0.06
10	590	NE	237	12	560	1.12	0.80±0.04
11	573	NE	226	18	520	1.38	1.52±0.38
12	578	NE	251	23	520	1.57	1.04±0.06
30	557	NEE	35	10	555	1.27	1.03±0.04
31	529	NEE	-	-	530	1.23	2.22±0.65
32	598	SW	120	32	560	1.40	1.16±0.11
40	553	SWW	185	11	560	1.27	1.14±0.13
41	520	SWW	185	12	520	1.40	1.49±0.10
44	521	NNE	288	10	560	1.20	1.69±0.30
46	539	N	236	24	560	1.06	1.53±0.22
ejecta							
42	592	N	-	-	-	-	1.56±0.40
45	571	NNE	-	-	-	-	1.25±0.66

Note: rim=direction of the site relative to the crater center; T_c =highest Curie temperature; I_{s1}/I_{s0} =ration of saturation magnetization befor and after thermomagnetic run; K_m =low-field magnetic susceptibility with standard deviation.

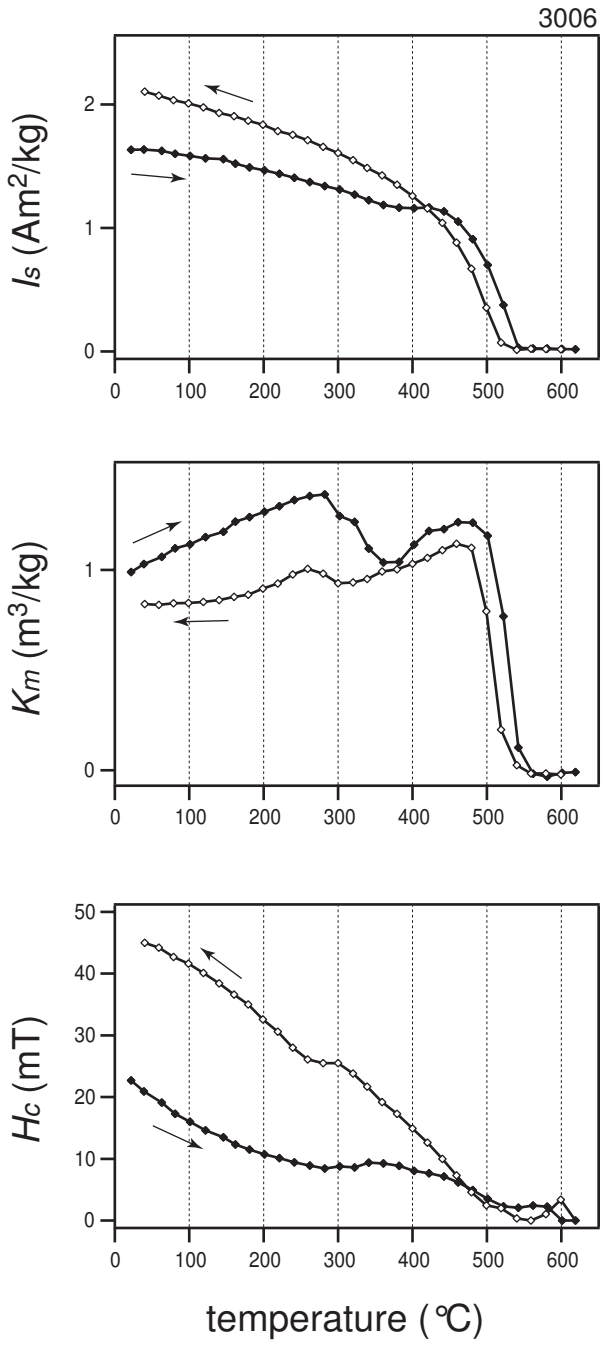

Figure 3.3: Typical example of temperature dependence of magnetic hysteresis properties: saturation magnetization (upper), low-field magnetic susceptibility (middle), and coercivity (bottom).

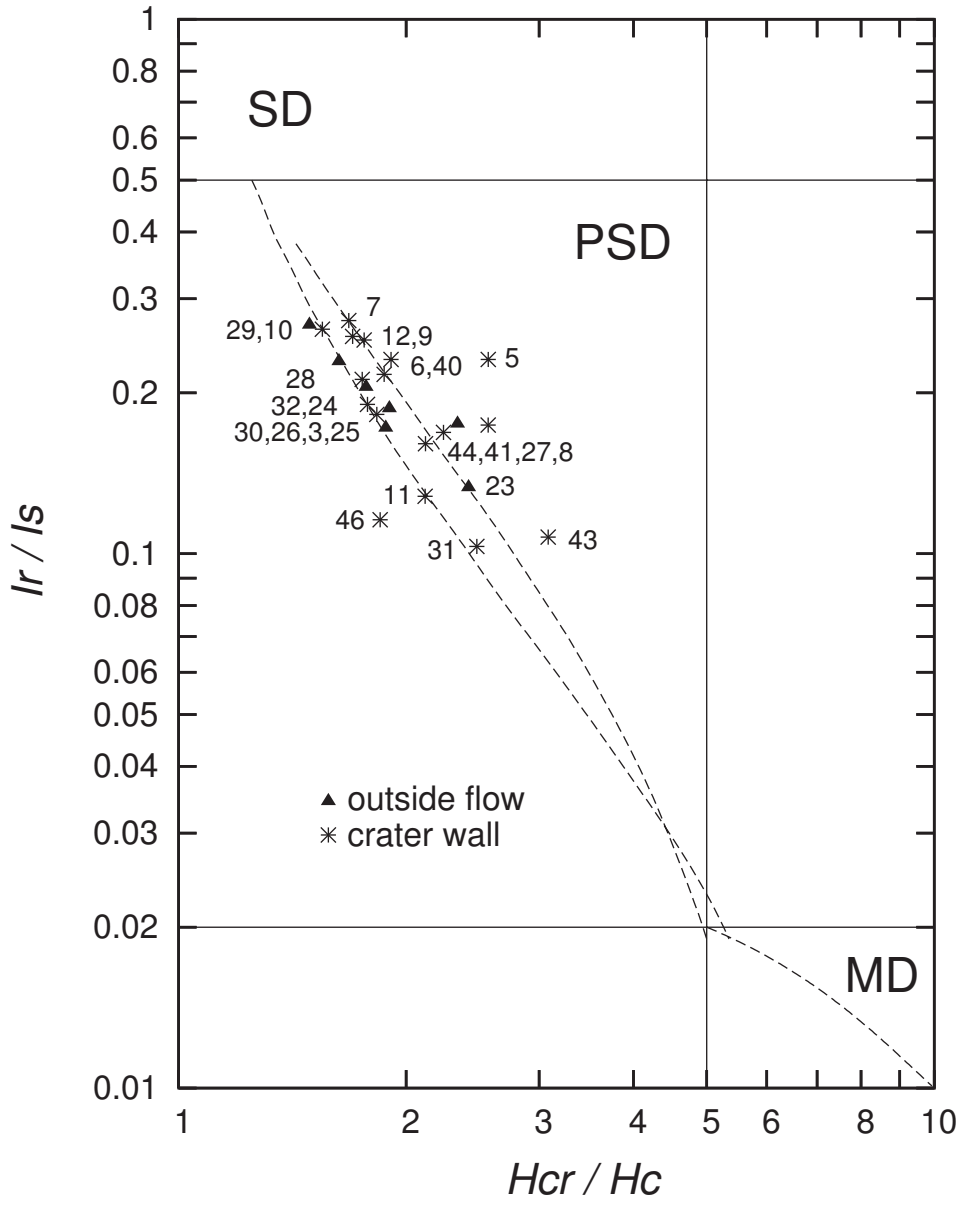

Figure 3.4: Plot of I_r/I_s versus H_{cr}/H_c (Day plot). The dotted lines indicate the master curves of the SD and MD mixing curves of magnetite [Dunlop, 2002].

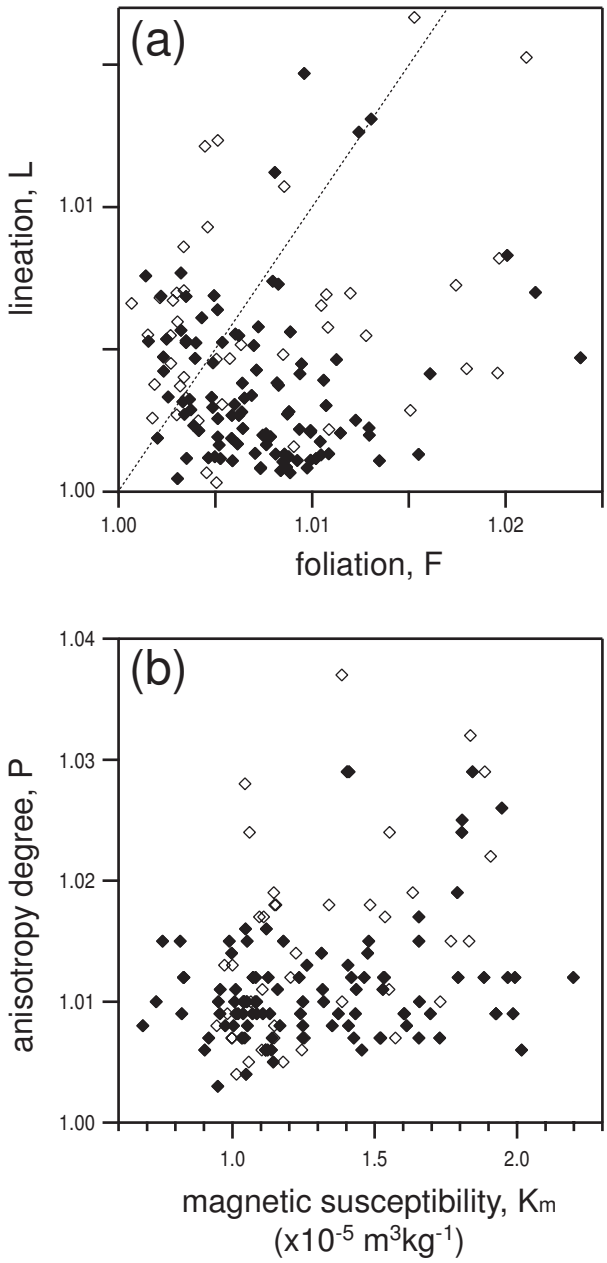

Figure 3.5: Plots characterizing the degree and shape of AMS ellipsoids. (a) Flinn-type plot. (b) Scatter diagram of anisotropy degree and the average low-field magnetic susceptibility. The solid and open symbols are data of the crater wall and outside samples, respectively.

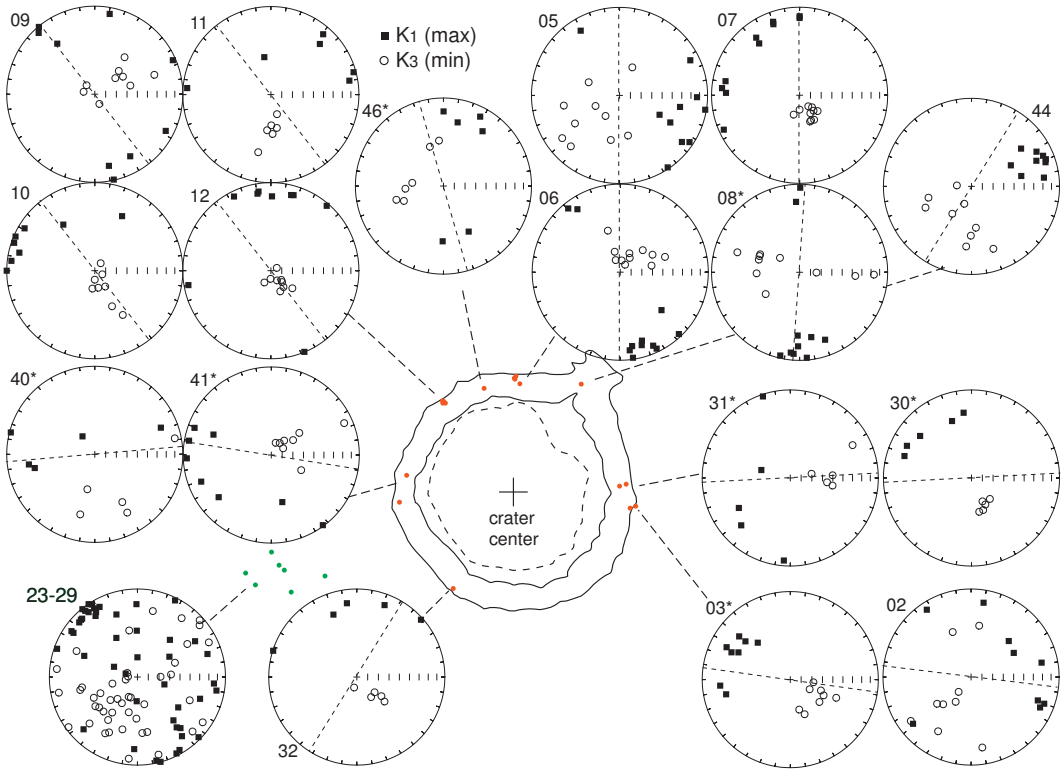

Figure 3.6: Equal-area lower hemisphere projections of the principal susceptibility axes. The intermediate axes were neglected because all the principal axes are orthogonal. The solid squares and the open circles indicate the maximum (K_1) and minimum (K_3) axes, respectively. The dashed lines indicate the radial direction of the sampling sites from the crater center. The number on the upper left of each figure indicates site number. The projections are after tilt correction, except for Site 31 where the tilting could not be determined. Asterisks indicate altitude less than 565 m (see Chapter 3.5).

of the outside flow are not shown in Fig. 3.5 because of their exceptionally high degree of anisotropy ($L = 1.04-1.05$, $F = 1.01-1.02$, P=1.060-1.064). Figure 3.5b shows that the P values of the most samples were less than 1.03 (<3%). Such foliated AMS with low anisotropy degree is typical of volcanic rocks [Tarling and Hrouda, 1993]. No or only weak positive correlation was observed between P and K_m for the inside and the outside flow sites, respectively.

3.4.4 Orientations of the principal susceptibilities

The orientations of the principal susceptibilities axes are plotted in Fig. 3.6. Many of the crater wall sites showed the minimum susceptibility (K_3) oriented vertically and the maximum susceptibility (K_1) in the horizontal plane. The K_3 axes are often tightly clustered, while the K_1 axes tend to be more scattered. This observation is consistent with the dominantly oblate shape of AMS ellipsoid (Fig. 3.5). For many of the sites, there is no strict parallelism between the maximum susceptibility and the radial direction from the crater center.

3.5 Discussion

3.5.1 Identification of magnetic minerals

Lonar basalts essentially contain Ti-poor titanomagnetite and its oxidized phase as the main magnetic minerals. The increase in I_s above 350°C is an indicative of inversion of titanomaghemite for poor-Ti composition [Özdemir, 1987]. During heating in air or in vacuum, metastable titanomaghemites invert to multiple intergrowths of the same bulk chemical composition. The variation in I_{s1}/I_{s0} indicates the differing composition and/or oxidation state of the starting titanomaghemite [O'Reilly, 1983].

Irreversible thermomagnetic curves were observed for all samples, including those from the flow outside the crater (Table 3.1). The similar feature has been reported for Deccan basalts in the other region [Kono et al., 1972; Shaw et al., 1991; Subbarao et al., 1989]. These facts prefer the interpretation that the low-temperature oxidation predated the impact event, at least to some extent.

The features around 300°C observed for K_m and H_c indicates the presence of magnetic minerals with small I_s and T_c at 350°C, as well as occurrence of some chemical or physical alteration. Because there is no drop in I_s at 300°C in the heating curve, the decrease in K_m might be in part due to irreversible

change in the domain structures rather than chemical alteration [Kosterov and Prevot, 1998]. It is uncertain whether this represent the beginning of inversion process. T_c at 350°C is probably due to presence of titanohematite, $xFeTiO_3$ $(1\text{-}x)Fe_2O_3$ with x = 0.45-0.55 [Westcott-Lewis and Parry, 1971]. The contribution of this mineral to K_m and, therefore to AMS, is insignificant relative to titanomagnetite/titanomaghemite.

3.5.2 AMS

The shock pressures in the basalt flows near the crater rim were probably less than those in the lower crater wall. This is due to not only pressure decays with distance, but also interference with rarefaction waves from the free surface [Melosh, 1989]. To evaluate effects of different shock pressure on AMS, we divided the sampling sites in the crater wall into two groups: upper (eight sites) and lower wall (nine sites). Altitude of 565 m is selected here as the boundary between the two groups, which also corresponds to the boundary between the fifth and fourth flow in the northern crater wall (Fig. 3.2).

The orientations of K_1 and K_3 for each group were compiled in Fig. 3.7, utilizing the Kamb [1959]'s contour method to visualize the statistical significance of the data. As expected from Fig. 3.6, the high concentration of K_3 is observed around the vertical axes for the crater wall (upper and lower), although those for outside is deviated about 40° from the vertical axis. The outside samples show a clear NW-SE trending magnetic lineation defined by the concentration of the K_1 axes. The upper wall samples show similar feature with more broad density contours. In contrast, the lower wall samples lack a strong magnetic lineation.

In Fig. 3.8, the K_1 and the K_3 axes of basalt in the crater wall were plotted with the radial directions being upward in the diagrams. A remarkable feature is the occurrence of a clear magnetic lineation for the lower flow, which is subparallel to the radial direction. This kind of agreement between AMS orientation and relative position in the crater has never been reported. In contrast to the lower flows, the lineation remained poorly defined for the upper flow.

The above fact prefers an interpretation that the expanding stress waves from the crater center produced new AMS in the lower flows with the K_1 axes parallel to the radial direction. This interpretation is supported by the result of the impact experiments (Chapter 2), where K_1 was induced parallel to

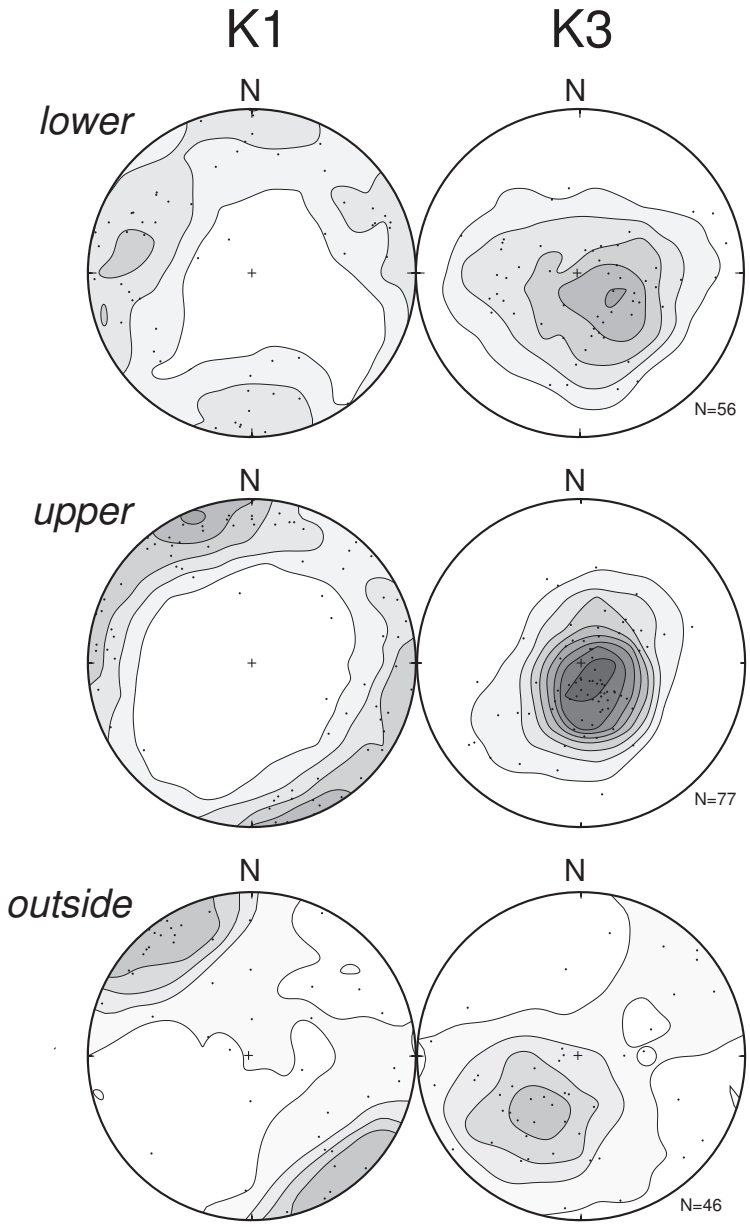

Figure 3.7: Equal-area lower hemisphere projections illustrating the orientation density of the K_1 and K_3 axes for three groups: upper wall, lower wall, and outside flow. The contours are drawn in intervals of 2σ, at the values 0, 2σ, 4σ, etc. [Kamb, 1959]. The expected density for no preferred orientation is 3σ. All the projections are after tilt correction, except for Site 03 (lower wall).

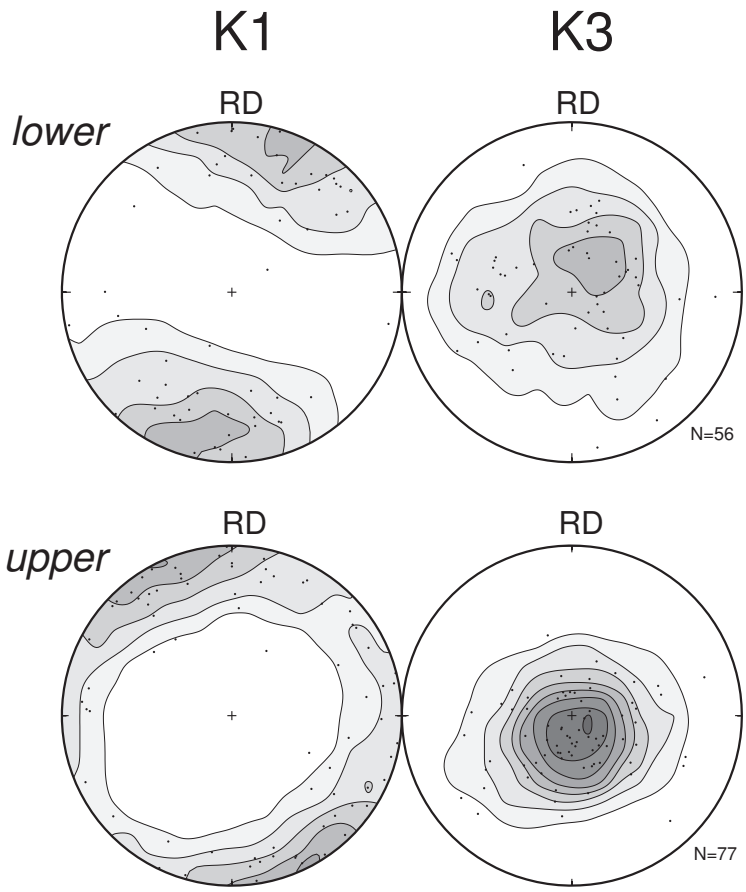

Figure 3.8: Same as Fig. 3.7 but the principal axes were rotated around the vertical axis in such a way that the radial directions (RDs) from the crater center are oriented upward.

shock direction at peak pressures around 0.4−3 GPa. Numerical calculations of impact cratering predict peak pressures around 1 GPa or less for the crater wall materials [e.g. Ugalde et al., 2005]. The above two estimated values of peak pressure are consistent to each other although the Ti-content of titanomagnetite is quite different between Lonar basalt and Omuro basaltic andesite. The result of the shock experiment also explains the following features of Lonar basalt in the crater wall: the low degree of anisotropy (Fig. 3.5) and the lack of exact parallelism between the K_1 axis and the radial direction (Fig. 3.6).

3.6 Conclusions

Magnetic mineralogy and AMS of basalt from the upper crater wall of Lonar crater were investigated. The result of the present study can be summarized as follows.

(1) Lonar basalt contains Ti-poor titanomagnetite and its oxidized phase (titanomaghemite) as the main magnetic minerals.

(2) Stress waves generated during the impact event likely produced new AMS in basalt in the upper crater wall (lower flows). The maximum principal axes are preferentially oriented horizontally along the substantially radial direction from the crater center.

Chapter 4

NRM of Lonar basalt

4.1 Experiments

We performed paleomagnetic measurements using a superconducting magnetometer (2G, SRM760) with an in-line static three-axis demagnetizer. Alternating field demagnetization was used to isolate components of natural remanent magnetization (NRM) because shock preferentially de/re-magnetizes low coercivity grains [Hargraves and Perkins, 1969; Pohl et al., 1975; Cisowski and Fuller, 1978]. Stepwise AFD was performed up to a peak alternating field of 80 mT, at 2.5 mT steps in a low field range and 5 or 10 mT steps in high field ranges. Stepwise thermal demagnetization was conducted for one sample from each site. Specimens were heated in air using a magnetically shielded furnace. The residual field during the cooling cycle was less than 50 nT. Results of the alternating field and thermal demagnetization were plotted on orthogonal vector diagrams [Zijderveld, 1967] to identify different NRM components, as well as on equal-area projections to evaluate directional stability. Least-squares regression was used to estimate magnetization lines or planes. We determined orientations of the soft NRM component using the data points below 12.5 mT. This is because the results of the previous shock experiments showed that SRM on basalt is removed in this field range [Pohl et al., 1975]. The sites-mean directions were determined using Fisher [1952]'s statistic for the most sampling sites, whereas the combined analyses of line and plane [McFadden and McElhinny, 1988] were used for a few sites where linearity of isolated components was relatively low. A series of analyses was carried out using Paleomac software package [Cogńe, 2003].

To estimate the magnetic hardness of the samples, stepwise alternating

field demagnetization of anhysteretic remanent magnetization (ARM) was conducted. ARM was imparted in an alternating field of 80 mT and a bias field of 0.05 mT.

4.2 Results

Alternating field demagnetization

Two NRM components were isolated from the majority of the samples from the crater wall, outside flow, and ejecta clasts (Fig 4.1). The soft component was removed by a peak alternating field of less than 15 mT. The stable component was then decayed linearly toward the origin of the orthogonal plot. The peak field of 80 mT demagnetized 70−95% of the initial NRM. The outside samples were generally less remagnetized than the inside samples, which did not allow us to determine the directions of the soft component. The ejecta samples showed varying degrees of remagnetization. Some samples showed significant remagnetization as shown in Fig 4.1(c), while some other samples displayed only one component.

Thermal demagnetization

The result of thermal demagnetization generally showed two (Fig. 4.1b,d) or, more commonly, three or four NRM components (Fig. 4.1a,b). In the former case, the low- and high-temperature component (LTC/HTC) are equivalent to the low- and high-coercivity components isolated by alternating field demagnetization, respectively. LTC was unblocked by 240°C, and then the HTC was unblocked by 520°−600°C. In the latter case, the NRM components unblocked at 200°−480°C might be spurious due to unblocking of both high- and low-coercivity components in the same temperature range. A few samples also showed the presence of another component unblocked at 480°−560°C (Fig. 4.1a). This small component is approximately antiparallel to HTC (or high-coercivity component), which might indicate self-reversal of remanent magnetization.

Most of samples showed large unblocking at 250°−300°C and at 500°−580°C (Fig. 4.1); The latter is related to unblocking of magnetite, whereas the former is either due to unblocking of titanohematite (Fig. 3.3) or inversion of titanomaghemite. Figure 4.2 shows the result of stepwise thermal demagnetization of ARM for two samples from the same site, in which one sample had

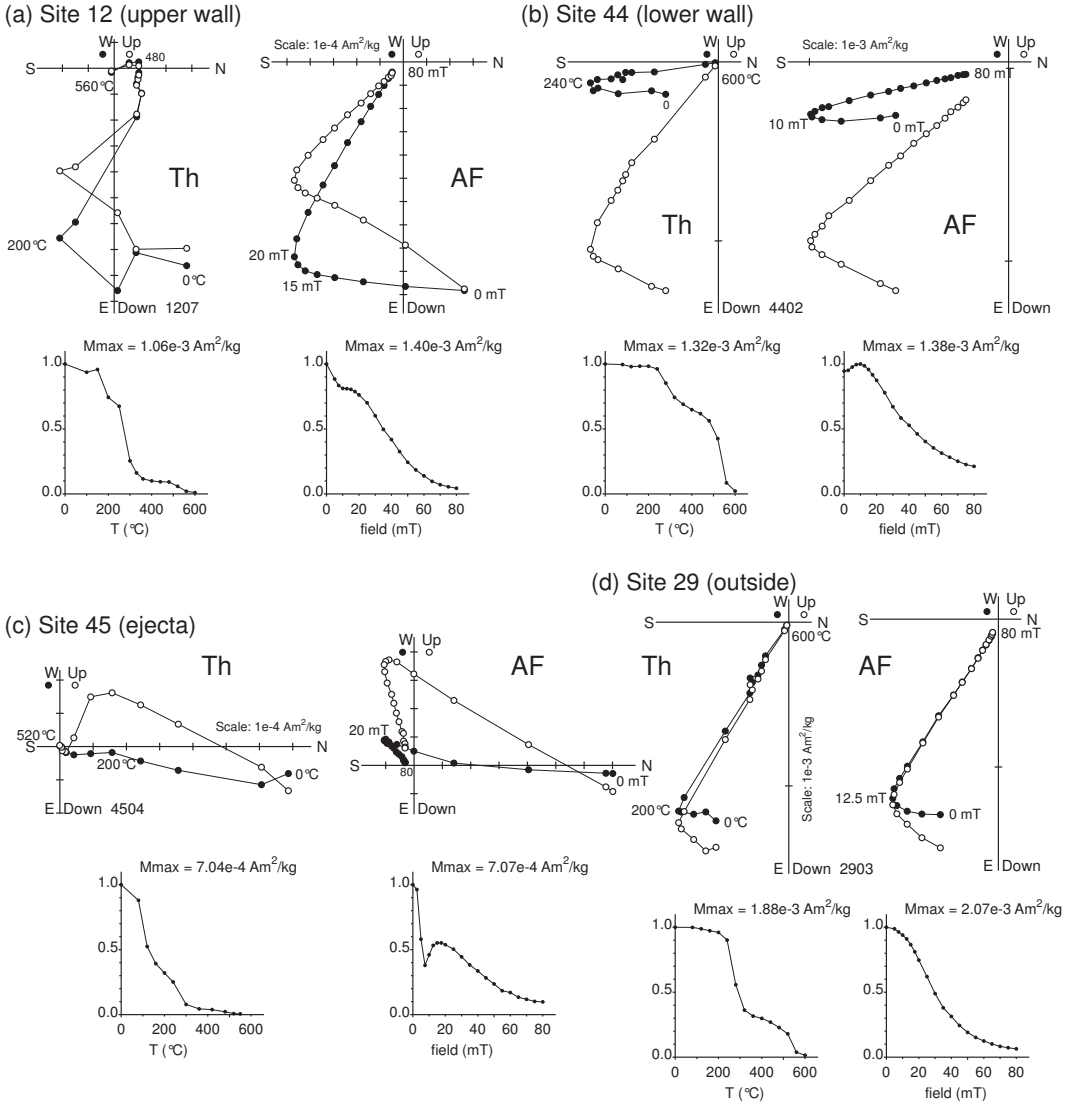

Figure 4.1: Typical orthogonal projections of magnetization vector end points during thermal and alternating field demagnetization. The results of two specimens from the same drill core are shown. Solid and open symbols are projection on to the horizontal and vertical plane, respectively. Projections in geographic (in situ) coordinates.

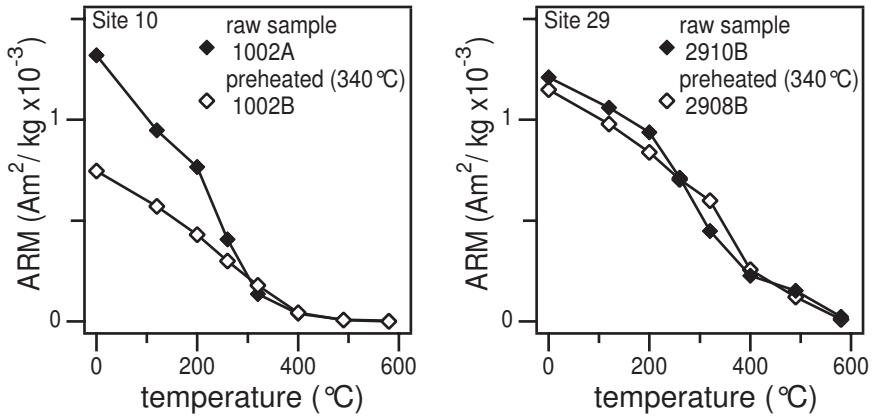

Figure 4.2: Stepwise thermal demagnetization of anhysteretic remanent magnetization (ARM). One sample was heated at 340°C and cooled down in advance before imparting ARM. The significant unblocking at 200°−300°C for the raw samples is absent for the pre-heated samples, indicating loss of NRM due to alteration of magnetic minerals.

been pre-heated at 340°C in air for 20 minutes. Only the raw samples showed significant unblocking of ARM at 200°−320°C, indicating titanomaghemite as the main carrier of NRM lost in the temperature range.

4.2.1 Intensity of the primary NRM component

Figure 4.3 shows intensities of residual NRM and ARM after AFD with a peak field of 15 mT (NRM_{15} and ARM_{15}, respectively) and median destructive field of ARM (MDF_{ARM}). Field intensity of 15 mT was selected here because the stable NRM component was usually isolated at this step. NRM_{15} was decreased toward the lower altitude although the value slightly increased at the lowest sites. The variation pattern of NRM_{15} was similar to that of NRM intensity presented in the previous study [Poornachandra Rao and Bhalla, 1984], although the authors plotted it as a function of distance from the crater center. The figure clearly shows that NRM_{15} is positively correlated with that of ARM_{15} and MDF_{ARM}, indicating that the intensity of the stable NRM component is dependent on the relative abundance of magnetic grains with high coercivity.

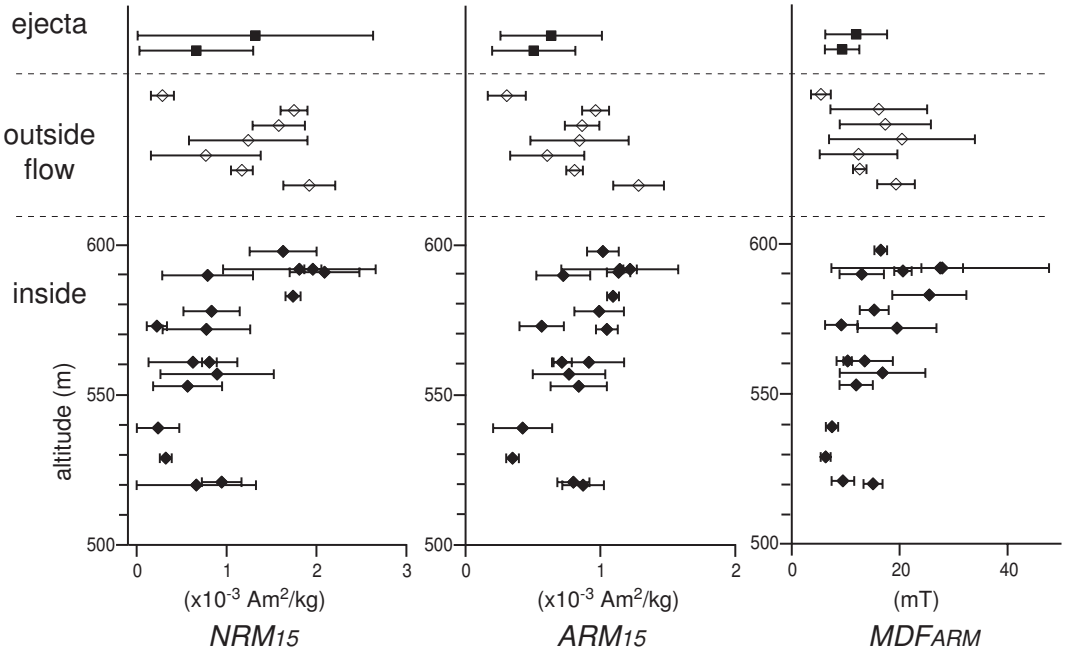

Figure 4.3: Plots showing variations in magnetic properties. NRM_{15} and ARM_{15} respectively indicate NRM and ARM after AFD with a peak field of 15 mT. MDF_{ARM} indicates the median destructive field of ARM.

4.2.2 Directional statistics

Innerwall

The site-mean orientations of the primary NRM component isolated by stepwise alternating field demagnetization are plotted in Fig. 4.4 and listed in Table 4.1. The site-mean of the upper wall sites showed an increase of Fisher's precision parameter, k, from 10.2 to 4.5 after tilt correction. This increase of k yielded the positive fold test of McElhinny [1964] at the 99% level. The fold test of McFadden [1990] was also positive at the 99% confidence level; the calculated value for $x1$ was 5.50 in the in situ coordinates and $x1$ is 0.05 after tilt correction, whereas the critical value at the 99% confidence level was xc=4.9. The overall-mean direction after tilt-correction was nearly parallel to that of basalts from outside the crater (Fig. 4.4, middle). These results conclude that the stable NRM component is the pre-impact magnetization, probably the primary remanence of basalt as previously believed. We have also confirmed that tilt-correction of the uplifted rim works properly.

In contrast, tilt correction did not improve the clustering of the site-mean directions of the lower wall sites. The variation is probably due to the secular

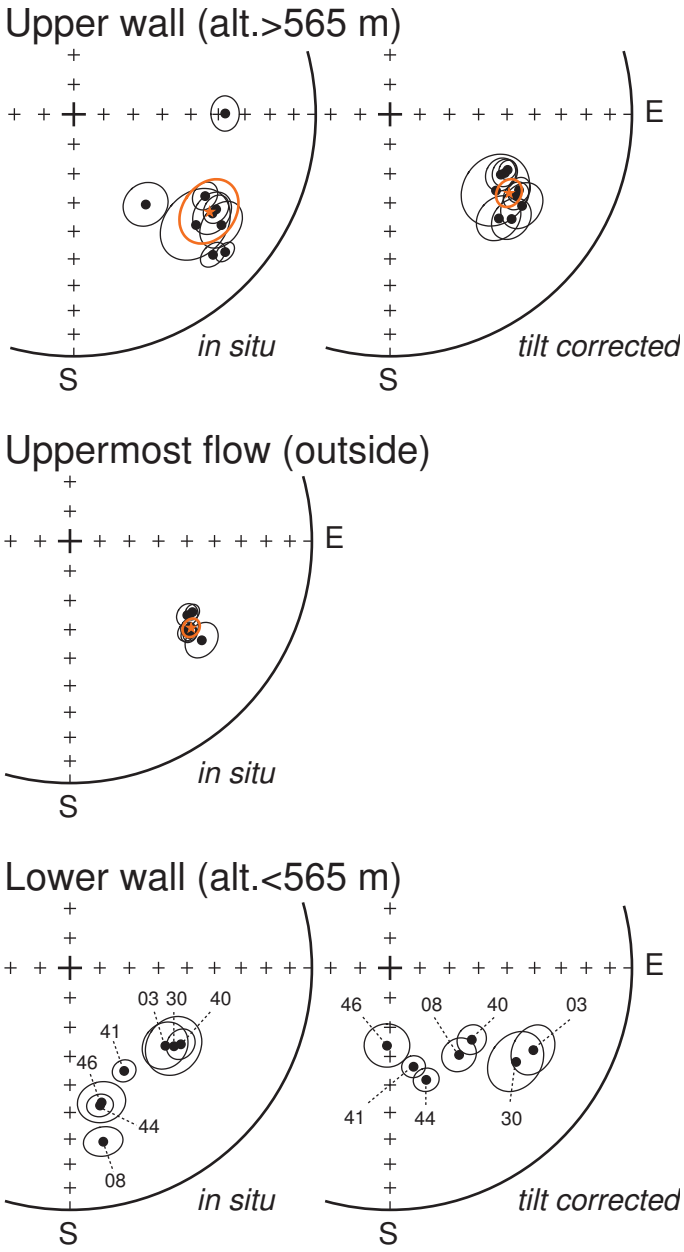

Figure 4.4: Equal-area projections showing the site-mean directions of the primary NRM component and the 95% confidence circles. A star with a 95% confidence circle indicates the overall mean direction. Solid symbols for the lower hemisphere and open symbols for the upper hemisphere.

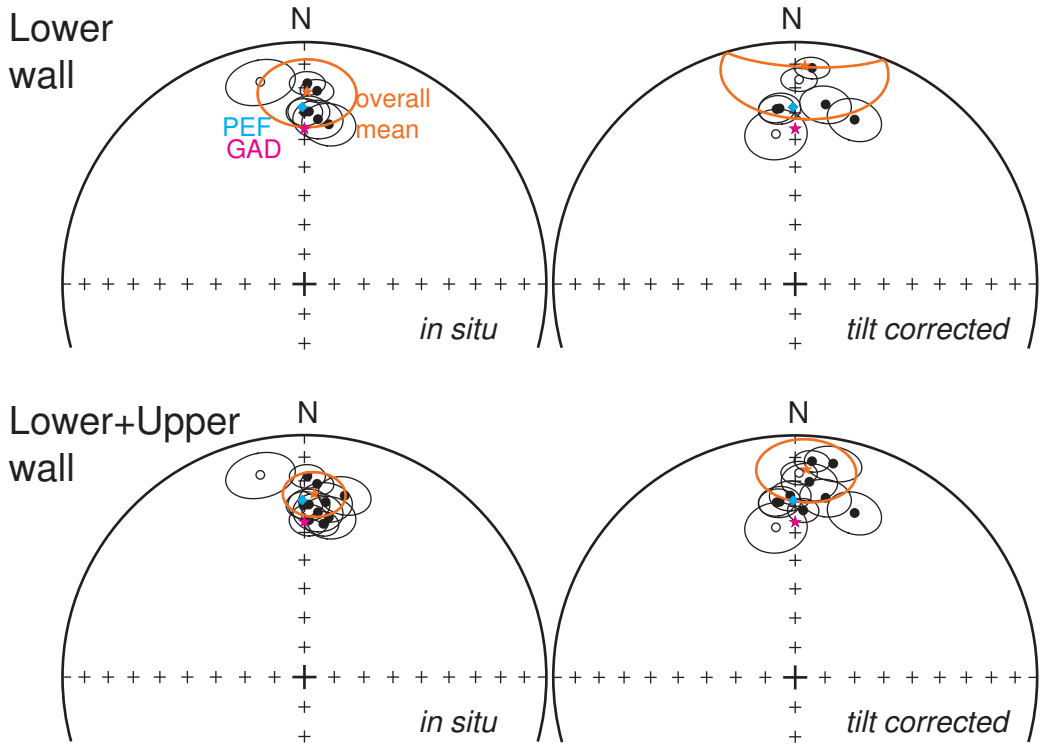

Figure 4.5: Same as Fig. 4.4, but for the soft NRM component. A blue diamond indicates the direction of the present earth field (PEF), while a magenta star indicates the direction of the geocentric axial dipole (GAD) field.

variation of geomagnetic field at the time of Deccan Trap emplacement. The site means directions of, for example, sites 41 and 44 are nearly parallel to each other and clearly deviated toward the south from those of the upper wall or outside flow. The two sites are located at the similar altitude of about 520 m, indicating that they correspond to the same flow. Paleomagnetic studies of Deccan basalt sequence [Kono et al., 1972] showed large scatter of the primary NRM directions. Paleosecular variation during the period was likely much larger than that of the present day [Vandamme et al., 1991].

The site-mean and the overall-mean directions of the soft NRM component are shown in Fig. 4.5 and listed in Table 4.2. The overall-means directions were calculated for both the lower wall sites (upper figure) and all the analyzed crater wall sites (lower figure). In both cases, the k value of the site-mean directions decreased after tilt correction. The statistical test of McElhinny was negative at 95% confidence level only in the case that the site-means of both the upper and lower wall sites are averaged. The fold test of McFadden was inconclusive in the both cases. The in-situ overall-mean directions were not distinguishable with the present local field direction at the 5% significance level. In contrast, Poornachandra Rao and Bhalla [1984] obtained the in-situ direction with declination of 9° and much higher inclination of 47° for the soft component. The difference of the average direction would be attributed to the small number of data they analyzed. The result of tilt correction prefers a conclusion that the soft NRM component is post impact remagnetization although the statistical test is not entirely conclusive.

Ejecta

The directions of the stable NRM component of ejecta clasts were largely scattered (Fig. 4.6). However, the component of fifteen out of 18 total samples had negative inclinations. This result indicates that the ejected flow(s) was overturned and also brecciated before or after the landing at the present site.

The soft component of some ejecta samples was poorly isolated by stepwise AFD. Thus we employed remagnetization circle method for AFD data between 2.5−12.5 mT to estimate the orientation of the soft component. Only two NRM components were identified for the majority of the samples; i.e. data points lie on one great circle. The convergent direction of the great circles [Halls, 1978] shown in Fig. 4.6 is close to that of the present earth field, indicating remagnetization after the ejection.

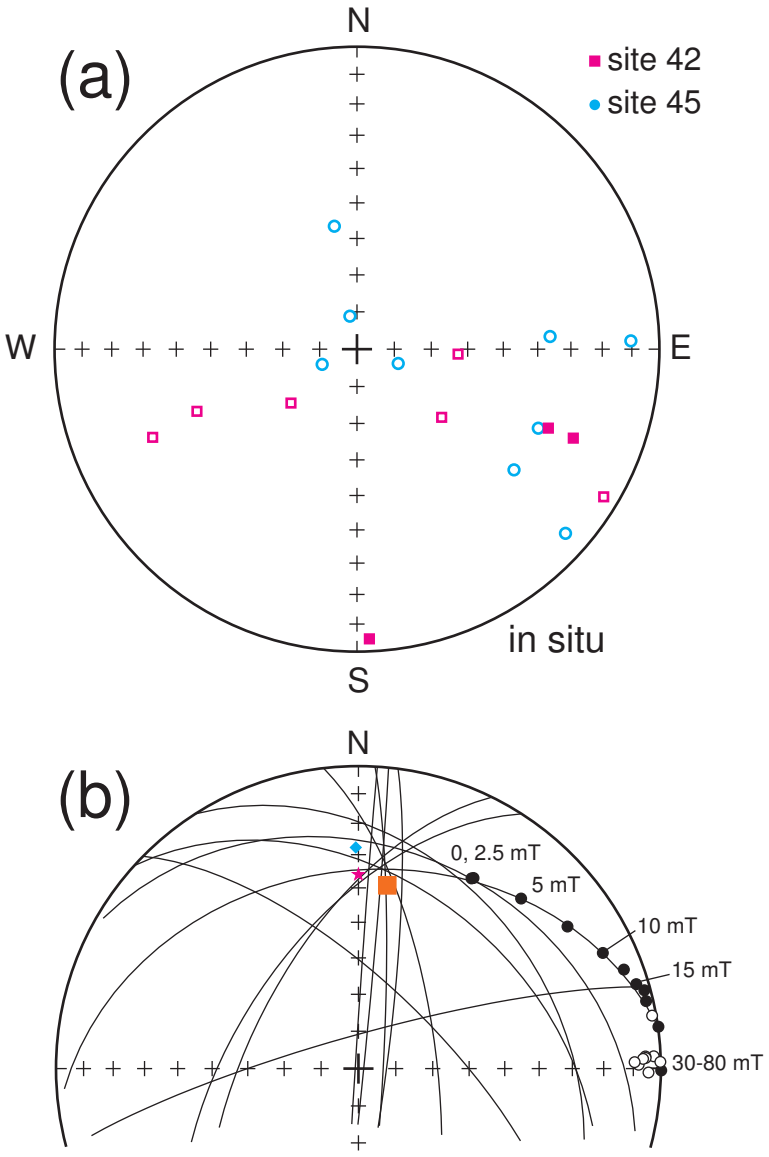

Figure 4.6: Result of paleomagnetic analyses for the ejecta samples. Equal-area, in-situ projections showing: (a) the orientations of the stable NRM component and (b) remagnetization circles projected on lower hemisphere. In figure (b), a typical example (specimen 4202B) of demagnetization behavior is shown. An orange square indicates the convergence orientation of the remagnetization circles. Solid symbols for the lower hemisphere and open symbols for the upper hemisphere.

Table 4.1: Summary of the high-coercivity (stable) NRM component.

Site	n	type	In situ		Tilt corrected		*k*	α*95*
			D (deg.)	I (deg.)	D (deg.)	I (deg.)		(deg.)
outside crater								
23	6	Fis.	127.0	32.3	-	-	141.8	5.6
24	7	Fis.	127.8	38.8	-	-	383.3	3.1
25	7	Fis.	127.9	37.6	-	-	473.9	2.8
26	6	Fis.	127.7	37.3	-	-	835.7	2.3
27	7	Fis.	122.3	42.2	-	-	270.0	3.7
28	7	Fis.	120.1	41.1	-	-	592.3	2.5
29	6	Fis.	125.8	38.9	-	-	488.3	3.0
mean	7	Fis.	125.6	38.3	-	-	415.3	3.0
innerwall (alt.>565 m)								
02	6	Fis.	141.4	50.6	133.7	37.8	82.8	7.4
05	7	Fis.	132.3	16.5	115.3	45.3	392.9	3.0
06	6	Fis.	135.3	19.4	120.4	38.1	281.8	4.0
07	5	Fis.	132.2	32.4	125.7	45.1	43.8	11.7
09	7	Fis.	125.6	30.3	130.7	34.1	82.7	6.7
10	5	Fis.	121.9	36.2	117.0	45.7	303.5	4.4
11	6	Fis.	126.9	24.7	124.7	34.0	85.6	7.3
12	5	Fis.	123.7	30.0	122.9	37.9	300.5	4.4
32	5	Fis.	89.7	37.5	118.6	46.7	209.5	5.3
mean	9	Fis.	125.7	31.5	-	-	26.6	10.2
mean	9	Fis.	-	-	123.5	40.7	134.6	4.5
innerwall (alt.<565 m)								
03	7	Fis.	129.2	47.8	119.8	32.3	61.7	7.7
08	6	Fis.	169.2	27.7	141.6	52.1	138.2	5.7
30	5	Fis.	127.0	45.3	126.7	35.3	64.4	9.6
31	5	Fis.	158.3	55.6	-	-	178.3	5.7
40	5	Mix	124.6	43.7	131.3	52.9	277.9	4.9
41	4	Fis.	152.2	50.2	166.6	55.5	578.4	3.8
44	4	Fis.	166.8	42.4	182.3	63.7	205.9	7.5
46	7	Mix	186.4	49.2	144.6	68.6	40.4	9.6

Note: n and type=number of specimens and types of analysis which were used to calculate the site-mean orientation, respectively; Fis.=Fisher statistics, or Mix.= mixed analysis of line and plane, D = declination, I = inclination, *k* = Fisher's precision parameter, α*95*= 95% confidence limit.

Table 4.2: Summary of the low-coercivity (soft) NRM component.

Site	n	type	In situ		Tilt corrected		*k*	α*95*
			D (deg.)	I (deg.)	D (deg.)	I (deg.)		(deg.)
innerwall								
03	6	Fis.	8.7	33.6	19.9	28.6	70.6	8.0
07	6	Fis.	12.5	24.2	10.1	11.2	80.1	7.5
08	6	Fis.	0.8	18.1	1.1	-16.6	189.3	4.9
10	4	Fis.	1.7	35.4	358.4	25.8	242.2	5.9
11	6	Fis.	6.9	28.0	4.2	20.1	75.9	7.7
12	5	Fis.	7.0	36.3	2.7	31.5	278.0	4.6
30	5	Fis.	4.7	32.2	9.6	25.7	108.7	7.4
40	5	Fis.	360.0	29.6	354.0	28.1	210.8	5.3
41	6	Fis.	1.5	29.4	354.9	28.0	123.1	6.1
44	7	Fis.	3.7	21.1	4.4	11.4	170.1	4.6
46	6	Fis.	347.7	-15.6	352.7	-37.5	51.6	9.4
mean	11	Fis.	3.1	25.2	-	-	27.5	8.9
mean	11	Fis.	-	-	3.1	15.0	12.7	13.3
*mean	7	Fis.	0.8	21.7	-	-	20.2	13.8
*mean	7	Fis.	-	-	2.5	10.5	8.6	21.8
ejecta								
42+45	13	conv.	9	38.6	-	-	-	-

Note: n and type=number of specimens and types of analysis which were used to calculate the site-mean orientation, respectively; Fis.=Fisher statistics, or Mix= mixed analysis of line and plane, D = declination, I = inclination, *k* = Fisher's precision parameter, α*95*= 95% confidence limit. The upper wall sites (>565 m) are excluded in the *mean.

4.3 Discussion

4.3.1 Intensity of the primary NRM component

Figure 4.3 shows a distinct decrease in the intensity of the primary NRM component (NRM_{15}) as the altitude of the sampling sites decreases. A similar variation pattern was shown for NRM intensity in the previous study [Poornachandra Rao and Bhalla, 1984], where they plotted it as a function of distance from the crater center. In the study, the authors explained that the result is due to shock demagnetization by stress waves decaying with distance.

However, difference in shock pressure cannot explain the high NRM intensity of the flow in the lowest part of the crater wall (Fig. 4.3). In addition, the correlation of NRM_{15} with ARM_{15} demonstrates that the intensity of the primary NRM is closely related to magnetic hardness. The result of the impact experiments (Chapter 2) showed that magnetic hardness is increased following the impact; i.e. stress wave should act to increase MDF_{ARM}. These results indicate that the observed variation in the intensity of the primary NRM component is related to the pre-impact magnetic properties, rather than shock demagnetization.The variation in the magnetic properties might be due to the different condition during the initial crystallization (e.g., cooling rate) or due to degrees of later low-temperature oxidation, or both.

Stress wave preferentially demagnetizes low-coercivity portion of remanence [Hargraves and Perkins, 1969; Pohl et al., 1975; Gattacceca et al., 2007] as shown in Fig. 2.7. Thus one would expect that the degree of demagnetization is larger in the lower flows because of their low magnetic hardness. The results of recent shock experiments on titanomagnetite-bearing rocks indicate that minimum shock pressure of 7 GPa [Gattacceca et al., 2007] or 1 GPa (Chapter 2) is required for significant demagnetization. Meanwhile, the peak shock pressures presumably did not exceed 1 GPa in the crater wall [Ugalde et al., 2005]. At the highest estimate, the stress wave with a peak pressures of $1-3$ GPa reduced the initial NRM_{15} only by 20% (Fig 2.7). The results of shock experiment cannot explain the large variation in NRM_{15}.

4.3.2 Origin of the low-coercivity NRM component

The result of unfolding suggests that a large part of the remagnetization occurred after the excavation of the crater. The soft NRM component in the crater wall showed the negative or inconclusive fold tests of McElhinny [1964]

and McFadden [1990], respectively. The in-situ overall mean direction was statistically indistinguishable from the PEF direction. The results of AFD for the ejecta samples also showed only two NRM components, in which the soft component is parallel to PEF (Fig. 4.6, 4.1c). These results indicate that no significant SRM was acquired by the innerwall and the ejecta samples.

A large part of remagnetization of Lonar basalt is explained by acquisition of viscous or thermoviscous remanent magnetization (VRM/VpTRM) after the impact. Acquisition of partial TRM by post shock heating is probably insignificant. Thermal demagnetization of innerwall and ejecta samples indicated that they were not heated above 200°C. Generally, TRM is largely blocked just below T_c, but only slightly in the low temperature range.

4.4 Conclusions

Natural remanent magnetization (NRM) of basalt from Lonar crater was studied. The result can be summarized as follows.

(1) Titanomagnetite and titanomaghemite are the main NRM carriers of Lonar basalt.

(2) The post-impact temperature in the crater wall and in the ejecta blanket did not exceed 200°C.

(3) The intensity of the primary NRM component is generally smaller in the lower part of the crater wall. The variation largely depends on the magnetic hardness of the flows rather than shock-related demagnetization.

(4) A dominant fraction of the soft NRM component was acquired after the excavation of the crater. They are presumably viscous or thermoviscous in origin.

Chapter 5

Discussion

5.1 AMS: an alternative tool to study impact crater

A remarkable feature of shock-induced AMS described in Chapter 2 is that AMS was produced at relatively low shock pressure. The minimum pressure of 0.4 GPa is much lower than that leading to formation of visible shock features in minerals. Shock features such as planar features in minerals, high-pressure polymorph, diaplectic and melt glass, is formed at shock pressures higher than 5 GPa. Such highly shocked materials are found just beneath the crater floor or as some ejecta clasts. The finding of the AMS changes in the upper crater wall of Lonar crater indicates the region where AMS is affected covers relatively large volumes of target rocks around impact craters.

The above features highlight the potential use of AMS as a sensitive indicator of the propagation direction of stress waves. The application of AMS to known terrestrial impact structures would provide new insight into the process of impact-related cratering, such as asymmetric pressure distribution by oblique impact [Dahl and Schultz, 2001; Pierazzo and Melosh, 1999]. AMS would be also used as an evidence of impact origin for suspected terrestrial impact structures.

We also note some potential restriction on the use of AMS to study impact crater: (1) AMS might not be induced by stress waves for rocks whose susceptibility is dominated by hematite, pyrrhotite, or paramagnetic minerals; (2) certain types of rock show high degree of initial anisotropy due to strong preferred orientation of magnetic minerals; in this case, the shock effect would be less significant.

A problem is that the mechanism of the shock-related AMS is uncertain at present. Further studies of AMS through shock experiments are clearly needed. For example, experiments using target rocks containing titanomagnetite with different Ti content might provide further insight into the relationship between magnetostriction and AMS, as magnetostrictive constant of titanomagnetite series is significantly increased with increased Ti content [Syono, 1965]. On the other hand, Irreversible changes in magnetic domain structures by stress waves would be observed using a Bitter pattern technique or a magnetic force microscopy.

5.2 Possible cause of magnetic anomaly of Lonar crater

Recent lunar and Mars magnetic data from the satellite observations revealed that the basaltic rocks outside the crater rims are partly demagnetized. Although it is interesting to see if the similar feature would be observed over Lonar crater, no aeromagnetic data has been unfortunately collected in this area. In this section, we discuss role of "rim materials" on magnetic anomalies that would be observed at Lonar and other terrestrial impact structures. This viewpoint is important for better modeling of magnetic structures observed at impact structures.

We could not obtain either evidence that basalt in the crater wall were demagnetized or remagnetized during the impact event. The result obtained in Chapter 4 concludes that the large part of remagnetization of Lonar basalt are viscous remanent magnetization (VRM) after the impact, whereas the large variation in the intensity of the primary NRM component is largely due to the variation in the primary (pre-impact) magnetic properties. Instead, we estimate that more potent cause of anomaly is the structural rim uplift. The tilting of the rim strata should have reoriented the vector of the NRM stable component at 30-40 degrees at a maximum. This effect should be taken into account in future aeromagnetic survey in this area.

Magnetization of rocks on the earth is a vector sum of the induced and remanent magnetization. Generation of new AMS should lead to change in induced magnetization. We note that magnetic anomaly at Lonar crater induced by this mechanism might be insignificant due to both the low anisotropy degree ($P<1.03$) and the large Königsberger ration (>1). However, it is still

unknown if AMS plays some role for anomalies observed at impact craters on crystalline rocks where induced magnetization is dominant. Thus shock-related AMS should be studied in future for other impact craters and through further laboratory impact experiments.

Chapter 6

Summary and Conclusions

Shock effects on magnetic properties were investigated through laboratory shock experiments and study of Lonar impact crater. Although previous shock experiment using terrestrial rocks described effect of strong shock on rock magnetic properties, effects of relatively weak shock (<5 GPa) were not studied in detail. In the present study, samples were sampled for magnetic measurements from a basaltic andesite block impacted with the initial pressure of 5 GPa, and also from basalt flows in the crater wall of Lonar impact crater. These specimens were subjected to detailed study of various magnetic properties, such as NRM, susceptibility, AMS, and hysteresis parameters.

NRM of basaltic andesite was partially but significantly demagnetized at peak pressures higher than 1 GPa. High-coercivity part of NRM, even higher than 80 mT, was partially demagnetized by the impact. At higher pressures (3-5 GPa), low-field magnetic susceptibility was significantly reduced and coercivity was increased, probably due to increased internal stress.

Different modes of change in AMS were observed at different distance from the impacted surface. The initial AMS was not significantlly changed by stresses less than 0.4 GPa. At around 0.4-3 GPa, the maximum susceptibility was induced parallel to the shock direction, and superposed on the initial AMS. This kind of changes in the AMS parameters was reported for the first time in this study. At higher pressures (>3 GPa), the anisotropy was increased, the minimum susceptibility was oriented toward the shock direction, and the average susceptibility was decreased. This feature at the highest pressure range is consistent with the result of a previous study.

No positive evidence of remagnetization or demagnetization of NRM was obtained for basalt in the crater rim. The variation in the intensity of the

primary NRM component was generally decreased with altitude in the crater wall. The relatively large secondary component was observed mainly for samples from the lower crater wall. The result of tilt correction revealed that the secondary NRM component was dominantly composed of a post-impact component. The intensity of the primary NRM remanence is likely related to the pre-impact magnetic properties of the flows.

On the other hand, the effect of stress waves on AMS was detected for basalts flows in the crater wall. The anisotropy degrees were not significantly different from those of basalt outside the crater rim. However, the maximum susceptibilities were oriented substantially (but not strictly) parallel to the radial direction. This feature was observed only for basalt in the lower part of the crater wall. This fact indicates that stress waves attained higher peak pressures in the lower crater wall.

References

Acuña, M. H., Connerney, J. E. P., Ness, N. F., Lin, R. P., Mitchell, D., Carlson, C. W., McFadden, J., Anderson, K. A., Rème, H., Mazelle, C., Vignes, D., Wasilewski, P., and Cloutier, P. (1999). Global distribution of crustal magnetization discovered by the Mars Global Surveyor MAG/ER experiment. *Science*, 284:790–793.

Akimoto, S., Katsura, T., and Yoshida, M. (1957). Magnetic properties of $TiFe_20_4$−Fe_3O_4 system and their change with oxidation. *J. Geomag. Geoelectr.*, 9:165–178.

Appel, E. and Soffel, H. C. (1985). Domain state of Ti-rich titanomagnetites deduced from domain structure observations and susceptibility measurements. *J. Geophys.*, 56:121–132.

Carporzen, L., Gilder, S. A., and Hart, R. J. (2005). Palaeomagnetism of the Vredefort meteorite crater and implications for craters on Mars. *Nature*, 435:198–201.

Chakrabarti, R. and Basu, A. R. (2006). Trace element and isotopic evidence for Archean basement in the Lonar crater impact breccia, Deccan Volcanic Province. *Earth Planet. Sci. Lett.*, 247(3-4):197–211.

Cisowski, S. M. and Fuller, M. (1978). The effect of shock on the magnetism of terrestrial rocks. *J. Geophys. Res.*, 83(B7):3441–3458.

Cogńe, J. P. (2003). Paleomac: A macintosh^{TM} application for treating paleomagnetic data and making plate reconstructions. *Geochem. Geophys. Geosyst.*, 4(1):1007. doi:10.1029/2001GC000227.

Collins, D. W., Melosh, M. J., and Ivanov, A. (2004). Modeling damage and deformation in impact simulations. *Meteorit. Planet. Sci.*, 39(2):217–231.

Dahl, J. M. and Schultz, P. H. (2001). Measurements of stress wave asymmetries in hypervelocity projectile impact experiments. *Int. J. Impact Eng.*, 26:145–155.

Day, R., Fuller, M., and Schmidt, V. A. (1977). Hysteresis properties of titanomagnetites: Grain-size and compositional dependence. *Phys. Earth Planet. Inter.*, 13:260–267.

Dunlop, D. J. (2002). Theory and application of the Day plot (Mrs/Ms versus Hcr/Hc) 1. Theoretical curves and tests using titanomagnetite data. *J. Geophys. Res.*, 107(3). doi:10.1029/2001JB000486.

Dunlop, D. J. and Özdemir, Ö. (1997). *Rock magnetism: Fundamentals and frontiers*. Cambridge University Press.

Earth Impact Database (2008). *http://www.unb.ca/passc/ImpactDatabase/*, (Accessed: Mar 2008).

Elbra, T., Kontny, A., Pesonen, L. J., Schleifer, N., and Schell, C. (2007). Petrophysical and paleomagnetic data of drill cores from the Bosumtwi impact structure, Ghana. *Meteorit. Planet. Sci.*, 42(4/5):829–838.

Fisher, F. R. S. (1952). Dispersion on a sphere. *Proc. Roy. Soc. London*, A 217:295–305.

Fredriksson, K., Dube, A., Milton, D. J., and Balasundaram, M. S. (1973). Lonar lake, India: An impact crater in basalt. *Science*, 180:862–864.

Fudali, R. F., Milton, D. J., Fredriksson, K., and Dube, A. (1980). Morphology of Lonar crater, India: Comparisons and implications. *The Moon and Planets*, 23:493–515.

Gattacceca, J., Boustie, M., Weiss, B. P., Rochette, P., Lima, E. A., Fong, L. E., and Baudenbacher, F. J. (2006). Investigating impact demagnetization through laser impacts and SQUID microscopy. *Geology*, 34(5):333–336.

Gattacceca, J., Lamali, A., Rochette, P., Boustie, M., and Berthe, L. (2007). The effects of explosive-driven shocks on the natural remanent magnetization and the magnetic properties of rocks. *Phys. Earth Planet. Inter.*, 162:85–98.

Halekas, J. S., Mitchell, D. L., Lin, R. P., Hood, L. L., Acuna, M. H., and Binder, A. B. (2002). Demagnetization signatures of lunar impact craters. *Geophys. Res. Lett.*, 29(13):23–1.

Halls, H. C. (1978). The use of converging remagnetization circles in paleomagnetism. *Phys. Earth Planet. Inter.*, 16:1–11.

Halls, H. C. (1979). The Slate Islands meteorite impact site: a shock remanent magnetization. *Geophys. J. R. astr. Soc.*, 59:553–591.

Hamuro, K. (1985). Petrology of the Higashi-Izu monogenetic volcano group. *Bull. Earthq. Res. Inst., Univ. Tokyo*, 60:335–440.

Hargraves, R. B. and Perkins, W. E. (1969). Investigations of the effect of shock on natural remanent magnetism. *J. Geophys. Res.*, 74(10):2576–2589.

Heider, F., Zitzelsberger, A., and Fabian, K. (1996). Magnetic susceptibility and remanent coercive force in grown magnetite crystals from 0.1 mm to 6 mm. *Phys. Earth Planet. Inter.*, 93:239–256.

Jackson, M., Borradaile, G., Hudleston, P., and Banerjee, S. (1993). Experimental deformation of synthetic magnetite-bearing calcite sandstones: effects on remanence, bulk magnetic properties, and magnetic anisotropy. *J. Geophys. Res.*, 98(B1):383–401.

Jelinek, V. (1981). Characterization of the magnetic fabric of rocks. *Tectonophysics*, 79(3-4):63–67.

Kamb, W. B. (1959). Ice petrofabric observations from Blue Glacier, Washington, in relation to theory and experiment. *J. Geophys. Res.*, 64:1891–1909.

Kapicka, A. (1983). Irreversible changes of anisotropy of magnetic susceptibility of rocks due to uniaxial pressure. *J. Geophys.*, 53(3):144–148.

Kapicka, A. (1988). Anisotropy of magnetic susceptibility in a weak magnetic field induced by stress. *Phys. Earth Planet. Inter.*, 51(4):349–354.

Kieffer, S. W., Schaal, R. B., Gibbons, R., Horz, F., Milton, D. J., and Dube, A. (1976). Shocked basalt from Lonar Impact Crater, India, and experimental analogues. *Proc. Lunar Sci. Conf. 7th*, pages 1391–1412.

Kono, M., Kinoshita, H., and Aoki, Y. (1972). Paleomagnetism of the Deccan Trap basalts in India. *J. Geomag. Geoelectr.*, 24:49–67.

Kosterov, A. A. and Prevot, M. (1998). Possible mechanisms causing failure of Thellier palaeointensity experiments in some basalts. *Geophys. J. Int.*, 134:554–572.

Kumar, P. S. (2005). Structural effects of meteorite impact on basalt: Evidence from Lonar crater, India. *J. Geophys. Res.*, 110(12):1–10. doi:10.1029/2005JB003662.

Mahoney, J. J. (1988). Deccan Traps. In J.D.Macdougall, editor, *Continental Flood Basalts*. Kluwer Academic Publishers, Dordrecht.

Maloof, A. C., Louzada, K. L., Stewart, S. T., and Weiss, B. P. (2005). Geology of Lonar crater, India: an analogy for Martian impact craters. *36th Lunar and Planetary Science Conference. (CD-ROM)*.

Marsh, S. P. (1980). *LASL Shock Hugoniot Data*. Univ. of Calif. Press, Berkeley.

McElhinny, M. W. (1964). Statistical significance of the fold test in palaeomagnetism. *Geophys. J. R. astr. Soc.*, 8:338–340.

McFadden, P. L. (1990). A new fold test for palaeomagnetic studies. *Geophys. J. Int.*, 103(1):163–169.

McFadden, P. L. and McElhinny, M. W. (1988). The combined analysis of remagnetization circles and direct observations in paleomagnetism. *Earth Planet. Sci. Lett.*, 87(1-2):161–172.

Melosh, M. J. (1989). *Impact cratering: A geologic process*. Oxford University Press, Oxford.

Mohit, P. S. and Arkani-Hamed, J. (2004). Impact demagnetization of the martian crust. *Icarus*, 168:305–317.

Murali, A. V., Zolensky, M. E., and Blanchard, D. P. (1987). Tektite-like bodies at Loner Crater, India: implications for the origin of tektites. *J. Geophys. Res.*, 92(B4):729–735.

Nakazawa, S., Watanabe, S., Iijima, Y., and Kato, M. (2002). Experimental investigation of shock wave attenuation in basalt. *Icarus*, 156:539–550.

Nakazawa, S., Watanabe, S., Kato, M., Iijima, Y., Kobayashi, T., and Sekine, T. (1997). Hugoniot equation of state of basalt. *Planet. Space Sci.*, 45(11):1489–1492.

Nishioka, I., Funaki, M., and Sekine, T. (2007). Shock-induced anisotropy of magnetic susceptibility: impact experiment on basaltic andesite. *Earth Planets Space*, 59:e45–e48.

O'Reilly, W. (1983). The identification of titanomaghemites: model mechanisms for the maghemitization and inversion processes and their magnetic consequences. *Phys. Earth Planet. Inter.*, 31:65–76.

Osae, S., Misra, S., Koeberl, C., Sengupta, D., and Ghosh, S. (2005). Target rocks, impact glasses, and melt rocks from the Lonar impact crater, India: Petrography and geochemistry. *Meteorit. Planet. Sci.*, 40(9-10):1473–1492.

Özdemir, Ö. (1987). Inversion of titanomaghemites. *Phys. Earth Planet. Inter.*, 46:184–196.

Park, J. K., Tanczyk, E. I., and Desbarats, A. (1988). Magnetic fabric and its significance in the 1400 Ma Mealy diabase dykes of Labrador, Canada. *J. Geophys. Res.*, 93(B11):13689–13704.

Pesonen, L. J., Deutsch, A., Hornemann, U., and Langenhorst, F. (1997). Magnetic properties of diabase samples shocked experimentally in the 4.5 to 35 GPa range. *In: Proceedings of the 28th Lunar and Planetary Science Meeting*, pages 1087–1088.

Pierazzo, E. and Melosh, M. J. (1999). Hydrocode modling of Chicxulub as an oblique impact event. *Earth Planet. Sci. Lett.*, 165:163–176.

Pilkington, M. and Grieve, R. A. F. (1992). The geophysical signature of terrestrial impact craters. *Rev. Geophys.*, 30:161–181.

Pohl, J., Bleil, U., and Hornemann, U. (1975). Shock magnetization and demagnetization of nasalt by transient stress up to 10 kbar. *J. Geophys.*, 41:23–41.

Poornachandra Rao, G. V. S. and Bhalla, M. S. (1984). Lonar Lake: palaeomagnetic evidence of shock origin. *Geophys. J. R. astr. Soc.*, 77(3):847–862.

Robertson, P. B. and Roy, J. L. (1979). Shock-diminished paleomagnetic remanence at the Charlevoix impact structure, Quebec. *Can. J. Earth Sci.*, 16:1842–1856.

Shaw, J., Sherwood, G. J., Mussett, A. E., Rolph, T. C., Subbarao, K. V., and Sharma, P. V. (1991). The strength of the geomagnetic field at the Cretaceous-Tertiary boundary: palaeointensity results from the Deccan Traps (India) and the Disko Lavas (Greenland). *J. Geomag. Geoelectr.*, 43(5):395–408.

Storzer, D. and Koeberl, C. (2004). Age of the Lonar impact crater, India: First results from fission track dating. *35th Lunar and Planetary Science Conference*.

Subbarao, K. V., Prasad, C. V. R. K., and Radhakrishnamurty, C. (1989). Alteration of magnetic minerals and its effect on the NRM of Deccan Trap flows of the Narmada region, India. *Earth Planet. Sci. Lett.*, 93:156–260.

Syono, Y. (1965). Magnetocrystalline anisotropy and magnetostriction of Fe_3O_4-Fe_2TiO_4 series, with special application to rock magnetism. *Japanese Journal of Geophysics*, 4(1):71–143.

Tarling, D. H. and Hrouda, F. (1993). *The magnetic anisotropy of rocks*. Chapman & Hall, London.

Ugalde, H. A., Artemieva, N., and Milkereit, B., editors (2005). *Magnetization on impact structures - Constraints from numerical modeling and petrophysics*. Large meteorite impacts III: Geological Society of America Special Paper 384. Geological Society of America.

Vandamme, D., Courtillot, V., Besse, J., and Montigny, R. (1991). Paleomagnetism and age determinations of the Deccan Traps (india): Results of a Nagpur-Bombay traverse and review of earlier work. *Rev. Geophys.*, 29(2):159–190.

von Frese, R. R., Potts, L., Gaya-Pique, L., Golynsky, A. V., Hernandez, O., Kim, J., Kim, H., and Hwang, J. (2006). Permian-Triassic mascon in Antarctica. In *Eos Trans. AGU, Jt. Assem. Suppl.*, volume 87, pages T41A–08.

Weihaupt, J. G. and Rice, A. (2007). Suggestions of multiple meteoroid impact in Antarctica: How do we sort it out? In *Antarctic Meteorites XXXI*, pages 103–104.

Westcott-Lewis, M. F. and Parry, L. G. (1971). Magnetism in rhombohedral iron-titanium oxides. *Aust. J. Phys.*, 24:719–734.

Zijderveld, J. D. A. (1967). A.C. demagnetization of rocks: analysis of results. In Collinson, D., Creer, K., and Runcorn, S., editors, *Method in Paleomagnetism*. Elsevier, Amsterdam.